NAVAL POSTGRADUATE SCHOOL

MONTEREY, CALIFORNIA

THESIS

RADAR CROSS SECTION (RCS) SIMULATION FOR WIND TURBINES

by

Cuong Ton

June 2013

Thesis Advisor: David C. Jenn
Second Reader: Ric Romero

Approved for public release; distribution is unlimited

THIS PAGE INTENTIONALLY LEFT BLANK

1. AGENCY USE ONLY *(Leave blank)*	2. REPORT DATE June 2013	3. REPORT TYPE AND DATES COVERED Master's Thesis	
4. TITLE AND SUBTITLE RADAR CROSS SECTION (RCS) SIMULATION FOR WIND TURBINES		**5. FUNDING NUMBERS**	
6. AUTHOR(S) Cuong Ton			
7. PERFORMING ORGANIZATION NAME(S) AND ADDRESS(ES) Naval Postgraduate School Monterey, CA 93943–5000		**8. PERFORMING ORGANIZATION REPORT NUMBER**	
9. SPONSORING /MONITORING AGENCY NAME(S) AND ADDRESS(ES) N/A		**10. SPONSORING/MONITORING AGENCY REPORT NUMBER**	

11. SUPPLEMENTARY NOTES The views expressed in this thesis are those of the author and do not reflect the official policy or position of the Department of Defense or the U.S. Government. IRB Protocol number ____N/A____.

12a. DISTRIBUTION / AVAILABILITY STATEMENT Approved for public release; distribution is unlimited	12b. DISTRIBUTION CODE A

13. ABSTRACT (maximum 200 words)

Wind-turbine power provides energy-independence and greenhouse-gas reduction benefits, but if wind turbines are built near military and commercial radar and communication installations, they can cause degradation in the systems' performance. The purpose of this research is to study the radar cross section (RCS) of a wind turbine and assess its effect on the performance of radar and communication systems. In this research, some basic scattering characteristics of wind turbines are discussed. Several computational methods of RCS prediction are examined, citing their advantages and disadvantages. Modeling and computational issues that affect the accuracy and convergence of the simulation results are discussed.

RCS simulation results for two wind turbine configurations are presented: a horizontal axis, three-blade design and a vertical axis helical design. Several methods of mitigating wind turbine clutter are discussed. Issues of RCS reduction and control for wind turbines are also addressed.

14. SUBJECT TERMS Radar Cross Section, wind turbine, simulation, model, surface meshing, RCS reduction, Lucernhammer, bistatic, monstatic, three-blade, helical, clutter, Doppler, numerical method.	15. NUMBER OF PAGES 93
	16. PRICE CODE

17. SECURITY CLASSIFICATION OF REPORT Unclassified	18. SECURITY CLASSIFICATION OF THIS PAGE Unclassified	19. SECURITY CLASSIFICATION OF ABSTRACT Unclassified	20. LIMITATION OF ABSTRACT UU

THIS PAGE INTENTIONALLY LEFT BLANK

RADAR CROSS SECTION (RCS) SIMULATION FOR WIND TURBINES

Cuong Ton
M. E., University of Utah, 1989

Submitted in partial fulfillment of the
requirements for the degree of

MASTER OF SCIENCE IN ELECTRICAL ENGINEERING

from the

**NAVAL POSTGRADUATE SCHOOL
June 2013**

Author: Cuong Ton

Approved by: David C. Jenn
                Thesis Advisor

                Ric Romero
                Second Reader

                R. Clark Robertson
                Chair, Department of Electrical and Computer Engineering

THIS PAGE INTENTIONALLY LEFT BLANK

ABSTRACT

Wind-turbine power provides energy-independence and greenhouse-gas reduction benefits, but if wind turbines are built near military and commercial radar and communication installations, they can cause degradation in the systems' performance. The purpose of this research is to study the radar cross section (RCS) of a wind turbine and assess its effect on the performance of radar and communication systems. In this research, some basic scattering characteristics of wind turbines are discussed. Several computational methods of RCS prediction are examined, citing their advantages and disadvantages. Modeling and computational issues that affect the accuracy and convergence of the simulation results are discussed.

RCS simulation results for two wind turbine configurations are presented: a horizontal axis, three-blade design and a vertical axis helical design. Several methods of mitigating wind turbine clutter are discussed. Issues of RCS reduction and control for wind turbines are also addressed.

THIS PAGE INTENTIONALLY LEFT BLANK

TABLE OF CONTENTS

THIS PAGE INTENTIONALLY LEFT BLANK

LIST OF FIGURES

THIS PAGE INTENTIONALLY LEFT BLANK

LIST OF TABLES

THIS PAGE INTENTIONALLY LEFT BLANK

LIST OF ACRONYMS AND ABBREVIATIONS

ACAD	Advanced Computer-aided Design
ATCR	Air Traffic Control Radar
CAD	Computer-aided Design
FDTD	Finite Difference Time Domain
FEM	Finite Element Method
GO	Geometrical Optics
GPS	Global Positioning System
GTD	Geometrical Theory of Diffraction
HF	High Frequency
LOS	Line-of-sight
MLFMM	Multilevel Fast Multipole Method
MoM	Method of Moments
MTI	Moving Target Indication
PEC	Perfect Electrically Conducting
PO	Physical Optics
PPI	Plan Position Indicator
PRF	Pulse Repetition Frequency
PRI	Pulse Repetition Interval
RAM	Radar Absorbing Material
RCS	Radar Cross Section
RF	Radio Frequency
RPM	Revolutions per minute
RRE	Radar Range Equation
SBR	Shooting and Bouncing Ray
SCR	Signal-to-Clutter Ratio
SNR	Signal-to-Noise Ratio
TDWR	Terminal Doppler Weather Radar
UHF	Ultra-high Frequency
UTD	Uniform Theory of Diffraction
VHF	Very High Frequency

THIS PAGE INTENTIONALLY LEFT BLANK

EXECUTIVE SUMMARY

In the global energy supply environment, the numbers of wind power installations are growing very rapidly each year. This means many wind turbines are installed close to microwave transmission and reception sites such as television, radio, radar, global positioning system (GPS), cellular and wireless networks. In many cases, because the receivers of these systems depend on detecting and processing very weak signals, wind turbines can interfere with the received signals. For example, the towers and blades of wind turbines have large scattering cross sections resulting in strong signals that can mask desired signals or saturate the receiver. Also, the rotating blades induce a Doppler shift that can degrade the processing gain. To assure a communication or radar system can operate effectively near wind power installations, it is necessary to conduct a detailed analysis, measurements, or simulations of the scattering characteristics of wind turbines.

The radar cross section (RCS) is a parameter that is used to estimate the effect of a wind turbine on a system's performance. Generally, a larger RCS indicates a more severe effect on the system's performance. A number of different factors can determine the RCS of a wind turbine:

- Material, size and shape
- Position of the rotor
- Frequency of the transmitted signal
- The incident angle where the transmitted signal hits a particular portion of the wind turbine
- Observation (receiver) angle (for the monostatic case the observation and incidence angles are the same; for the bistatic they are different)
- The polarization of transmitted signal and the polarization of the receiver antenna.

The objectives of this thesis are:

1) To identify some basic scattering characteristics of wind turbines
2) To discuss several computational methods of RCS prediction and cite their advantages and disadvantages

3) To conduct RCS simulations and show the results for two wind turbine configurations: a horizontal axis, three-blade design and a vertical axis helical design

4) To show methods of mitigating wind turbine clutter

5) To address issues of RCS reduction and control for wind turbines by way of geometric shaping and surface material selection known as radar absorbing material (RAM).

Some basic scattering characteristics of wind turbines are:

1) Wind turbine RCS varies with time because of the blade rotation and the associated change in multipath due to this rotor motion.

2) Wind turbine RCS is a non-linear function of angle, frequency and rotor position and has a relatively high forward scatter RCS that increases with frequency.

3) For the tall metal towers of wind turbines, the RCS is dominated by the tower scattering.

4) Bragg scattering can be observed at high frequency (HF) and very high frequency (VHF). The Bragg effect is coherent scattering from periodic scatterers.

Methods of RCS prediction include:

1) Method of moments (MoM) solutions of integral equations in the frequency domain;

2) The finite difference, time-domain (FDTD) solution of the differential equations in the time domain;

3) The finite element method (FEM) in both the time and frequency domains;

4) Approximate HF methods based on geometrical optics (GO) or physical optics (PO) and their edge diffraction extensions. In the case of GO, the geometrical theory of diffraction (GTD) is used; for PO, the physical theory of diffraction (PTD) is used;

5) Hybrid solution methods that include the shooting and bouncing ray (SBR) method;

6) Mixed solutions methods that use MoM, PO, GO, and edge diffraction. They can be applied to different portions of the object.

The bistatic and monostatic RCS was computed for both wind turbine configurations: a horizontal axis, three-blade design and a vertical axis helical design. Four frequencies were considered: 400 MHz, 900 MHz, 2.4 GHz and 5 GHz. The following is a summary of the simulation results:

- For bistatic RCS, most forward scattering comes from the tower, and the back scattering comes from the side of the nacelle

- For bistatic RCS, the forward scatter lobe increases with frequency and is orders of magnitude larger than the backscatter

- At a frequency of 400 MHz, Bragg scattering occurs and comes from a vertical blade and tower

- The sidelobe structure of the tower is visible at the frequency of 400 MHz;

- The reduction in RCS by using non-conducting blade materials (e.g., fiber glass) is not significant

- To mesh the wind turbine computer model for the simulation, a quadrilateral/triangular mesh has the same accuracy as a fine triangular mesh but uses only 3.7% of the fine mesh's number of facets. The reduction saves computational time when calculating the RCS for the entire wind turbine.

In a noise limited case an appropriate measure of radar and communication system performance is the signal-to-noise ratio (SNR). In the wind turbine case, the signal-to-clutter ratio (SCR) is used as the basis for performance evaluation (i.e., the noise is neglected in comparison to the clutter). Clutter is defined as unwanted signals that interfere or mask the desired signal.

The SCR cannot be increased by increasing the transmitter power because the clutter power also increases along with the target power. In order to increase the SCR, aside from reducing the wind turbine RCS, the sidelobe levels of both transmit and receive antennas should be as low as possible so the gain is lower in the direction of the

wind turbine. Also, it is advantageous to operate the antenna system in a direction where the wind turbine RCS is low. In the case of radar, if possible, it should operate in a condition where the target range is short and out of sight of the wind turbine (non line-of-sight).

To avoid aliasing (a phenomenon whereby the higher frequencies are mistaken for lower frequencies) of the Doppler frequencies induced by the rotating blades, the radar must sample the scattered signal at a rate greater than the Nyquist sampling rate. Nyquist sampling requires more than twice the samples per period of the highest Doppler shift present in the scattered signal. Also, the motion from the rotating turbine blades and its large time-varying RCS causes a Doppler shift that can interfere with the receiver processing.

RCS reduction was investigated. Geometric shaping and surface material selection known as RAM are two ways to reduce and control wind turbine RCS.

Shaping applied to the tower and nacelle could be effective, but it would have to be done with knowledge of the transmitter and receiver directions. Although it could reduce the RCS in some desired directions, it would likely increase it in others.

Surface materials selection and coatings require adding RAM to the surface of the wind turbine blades. RCS reduction is accomplished by reducing reflections and scattering from the edges of the blade. One way is by absorption, which refers to the transfer of energy from the wave to the material as it passes through the medium. The second way is by cancellation of multiple reflections, or destructive interference, where the coating properties are selected so that reflections from the front and back faces of a layer cancel. However, this may add weight to the platform and can affect its aerodynamic performance.

In most situations the aerodynamic degradation and cost does not justify the use of RAM because of the relatively small reduction in RCS that is provided. An exception might be where the radar and communication systems operate near a wind farm, in which case shaping and RAM can be used effectively.

Most commercial RAM materials give a RCS reduction in the range of 15 to 20 dB; however, it varies widely with bandwidth, frequency and angle of incidence. A RAM coating might make sense if the wind turbine was near an airport where air traffic control radar and terminal Doppler weather radars are located. From the simulation results of wind turbine RCS, the reduction in RCS by using non-conducting blade materials (fiber glass) was not significant.

THIS PAGE INTENTIONALLY LEFT BLANK

ACKNOWLEDGMENTS

THIS PAGE INTENTIONALLY LEFT BLANK

I.   INTRODUCTION

A.   BACKGROUND

For many centuries, wind-powered machines have been used to pump water and grind grain. With the development of electric power, wind power generators have been used to provide electricity to buildings and sailboats. Since the early 1900s, many wind turbines have been developed and used commercially. Because of the increasing global demand for energy, wind-turbine power is becoming more popular in the U.S. and Europe. Large-area installations of wind turbines called "wind farms" are being installed throughout the world. Certainly, wind-turbine power provides energy-independence and greenhouse-gas reduction benefits, but if wind farms are built near military or commercial radar and communication installations, they can cause degradation in the systems' performance.

Wind turbines harvest wind energy and convert it into usable power which can produce electricity. There are two basic types of wind turbines: horizontal axis wind turbines and vertical axis wind turbines. A picture of a three-blade, horizontal axis wind turbine is shown in Figure 1.

As shown in Figure 1, the blades are faced in the direction of the wind and rotate around a horizontal axis when pushed by the wind, and the turbine converts the wind's kinetic energy into electrical energy. The three-blade horizontal axis wind turbine is effective because it can produce megawatts of electrical power and takes up only a small area of land. Collections of these are ideal for large-scale power generation and are known as wind farms. The largest wind farms are found offshore. A typical horizontal axis wind turbine can generate up to 2 MW of electrical power. The dimensions of some commercial horizontal axis wind turbines are listed in Table 1.

Figure 1. This photo shows a three-blade, horizontal axis wind turbine installation.
(From [1]).

Table 1.   The dimensions of some commercial horizontal axis wind turbines.
(From [1–3]).

Output Power	Rotor Diameter (m)	Rotor Speed (rpm)	Tower Length (m)
1.8 MW	80	16.8	60
1.5 MW	77	18.1	80
1 MW	55	21.95	68

A second basic type is the vertical axis wind turbine. Most modern vertical axis wind turbines have a helical blade design. This design is more efficient and generates little vibration which can help to reduce noise levels. A picture of a helical design vertical axis wind turbine is shown in Figure 2.

As shown in Figure 2, the helical blades spin parallel to the ground so that they can operate anywhere regardless the wind direction. The advantages of vertical axis

helical wind turbines are their small size, quietness, and low cut-in wind speeds to generate electrical power. They are ideal for small-scale power generation and mostly found on the ground and on rooftops of residential and urban areas. A typical vertical axis helical wind turbine can generate up to 6.5 kW of electrical power. The dimensions of some commercial vertical axis helical wind turbines are listed in Table 2.

Figure 2. A vertical axis wind turbine installation. (From [4]).

Table 2.   The dimensions of some vertical axis helical wind turbines. (From [5–7]).

Output Power	Rotor Diameter (m)	Tower Length (m)
6.5 kW	3.1	5.5 (roof mounted) 18 (ground mounted)
2.5 kW	1.9	6 (roof mounted) 18 (ground mounted)
1.5 kW	2.8	4 (roof mounted) 18 (ground mounted)

Consider the scenario shown in Figure 3. Both monostatic and bistatic geometries are among the applications shown in the figure. Monostatic radar is where the transmitter and receiver are co-located and often share the same antenna. An example of monostatic radar is the air traffic control (ATC) radar or the terminal Doppler weather radar

(TDWR). A bistatic radar system implies that the transmitter and receiver are at different locations when viewed from the target. Bistatic radar is not as common as monostatic radar; however, the general bistatic case includes broadcast systems, cellular radio, and the global positioning system (GPS).
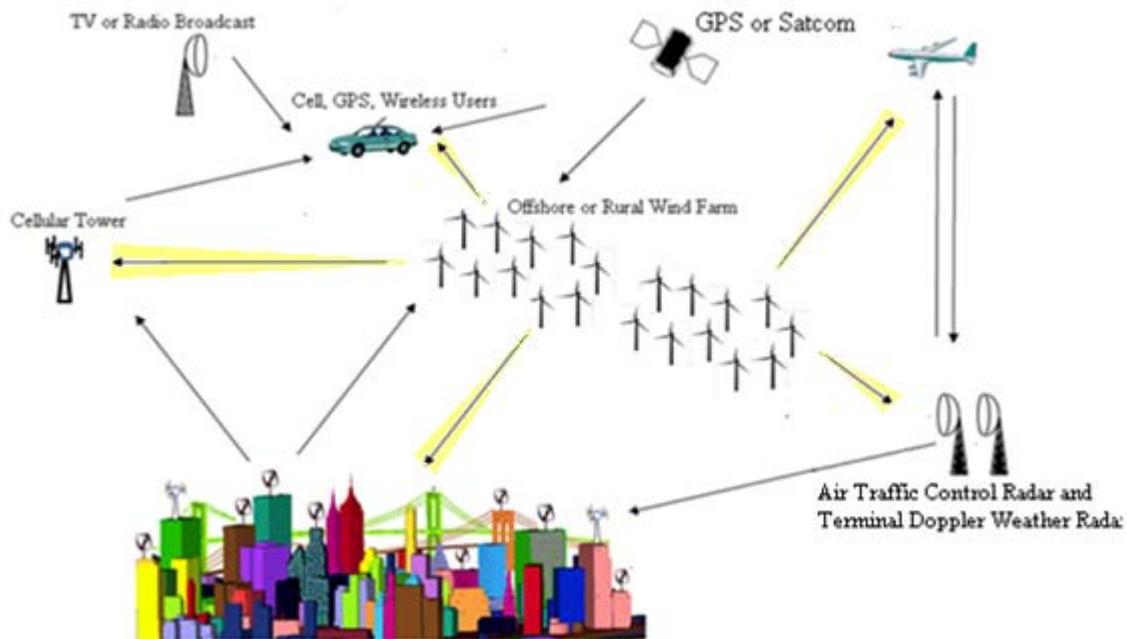
Figure 3. This general scenario shows many electronic communication and sensor systems operating near wind farms.

In the scenario shown in Figure 3, it may be difficult to detect and track targets near the wind farm because the radar signal scattering from a wind farm can be much larger than most target returns. As illustrated in Figure 4, the wind turbine rotating blades create time-varying Doppler spectra which can prevent radar from filtering rotor returns. Even in the case where the target is outside of the wind farm area, strong returns from the tower and blades of wind turbines can mask weak target returns. Moving targets can be mistaken for weather echoes because the rotating blades induce a Doppler spread that can mask target returns. Also, because of the characteristics of wind turbine scattering, the radar may not recognize a scattered target signal and process it as clutter.
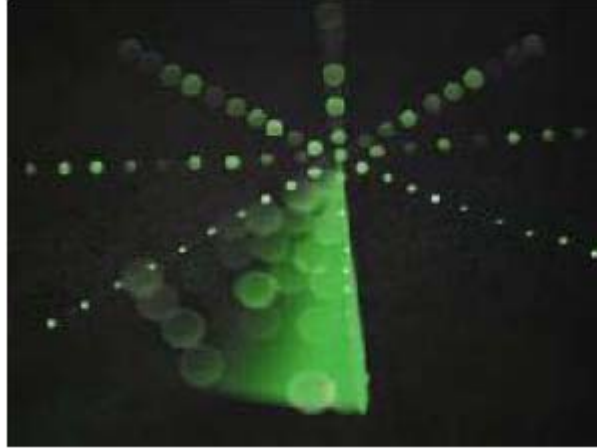
Figure 4.   The interference pattern caused by wind turbines is displayed on the surveillance radar Plan Position Indicator (PPI). (From [8]).

B.   PREVIOUS WORK

The radar cross section (RCS) is a measure that can be used to estimate the effect of a wind turbine on a system's performance. Many studies have been performed evaluating the RCS of wind farms and their effect on radar and communication systems. Studies on wind turbine impact on radar performance are presented in [9–13]. In [14–16] are shown measurements, either in the field or in a measurement facility, to estimate the wind turbine scattering and its impact on radar performance. The general problem of radio frequency (RF) installations with wind turbines in the near field of the antenna is described in [17]. The interference with digital television reception is specifically discussed in [18], and the reduction and control of wind turbine RCS, in order to minimize interference with RF systems, is covered in [19], [20].

C.   OBJECTIVE

In this thesis, some fundamental scattering characteristics of wind turbine RCS are described. All previous publications have addressed only the monostatic RCS of horizontal axis wind turbines. Not only the monostatic RCS but the bistatic RCS, which is of interest to assess the impact of wind turbines on communication systems, is addressed in this thesis. Communication, broadcast and cellular systems almost always

5

operate in a bistatic scenario, as illustrated in Figure 3. Also, the RCS of the vertical axis helical windmill is presented.

This thesis is organized into eight chapters. Wind turbine history and technologies are introduced in Chapter I. In Chapter II, the RCS is defined, and the basic range equations for predicting the scattered power from a wind turbine are shown. In Chapter III, several computational methods that can be used to predict RCS are described, citing their advantages and disadvantages. In Chapter IV, RCS simulation results are presented for the three-blade horizontal axis wind turbine configuration. Examples of Doppler effects from a wind turbine rotor are discussed. In Chapter V, RCS simulation results are presented for the vertical axis helical wind turbine configuration. In Chapter VI, modeling and computational issues that affect the accuracy and convergence of the simulation results are discussed. In Chapter VII, methods of wind turbine clutter prediction are presented. The issues of RCS reduction and control for wind turbines are addressed. Finally, Chapter VIII includes a summary of the results, conclusions, and recommendations for future research.

II.   RCS AND RANGE EQUATIONS

In this chapter, the radar cross section and radar range equation (RRE) are presented. The signal-to-clutter (SCR) ratio is discussed for the monostatic and bistatic scenarios. The SCR is used as the basis for radar and communication systems performance evaluation.

RCS is a measure of the power scattered in a specific direction when a target is illuminated by a plane wave, normalized to the power density of the incident field. The normalization makes the RCS calculation independent of the distance between the illumination source and target. Mathematically, the RCS of a point target (i.e., a target that is much less than the size of the radar resolution cell) is defined as [21], [22]

$$\sigma_{pq}(f,\theta_i,\phi_i,\theta_s,\phi_s) = \lim_{R\to\infty} \frac{4\pi R^2 \left|E_p^s(\theta_s,\phi_s)\right|^2}{\left|E_q^i(\theta_i,\phi_i)^2\right|}, \tag{1}$$

where R is distance from the target, f is the frequency, E is the electric field, the superscript i denotes incident, s denotes scattered, and the subscripts $p,q = \theta$ or ϕ are the components in a spherical polar coordinate system, as shown in Figure 5. The limiting process in (1) assures that the scattered field is proportional to $1/R$. The case where $p = q$ is referred as the co-polarized RCS, whereas the cross-polarized RCS is when $p \neq q$. In general, σ is written as a scalar, and the functional dependencies of frequency and angle are not included. The unit is typically m^2 or the decibel unit dBsm defined by

$$\sigma, \text{dBsm} = 10\log_{10}(\sigma, m^2). \tag{2}$$
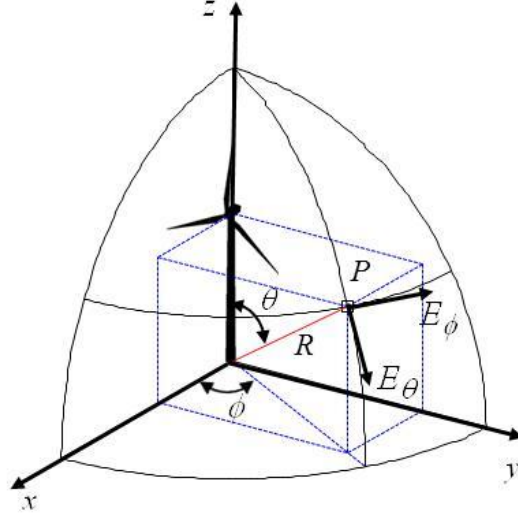
Figure 5. The coordinate system used for wind turbine RCS pattern analysis.

In the monostatic case, as illustrated in Figure 6, the received power from a target at range R is given by the radar range equation [23]

$$S = \frac{P_t G_t^2 \lambda^2 \sigma_t}{(4\pi)^3 R^4 L} |F_t|^4 \tag{3}$$

where P_t is the transmitter power, G_t the antenna gain in the direction of the target, λ the wavelength, σ_t the target RCS (m^2), and L is a miscellaneous system loss factor. The factor F_t is the one-way voltage path gain (propagation) factor and is squared to obtain power and squared again for a round trip, resulting in the fourth power. The path gain factor is a complex quantity that accounts for the relevant propagation modes between the radar and target. In general, because most of the systems under consideration operate near the ground, it will include multipath (or "ground bounce"). It will also include losses due to precipitation and foliage.

8
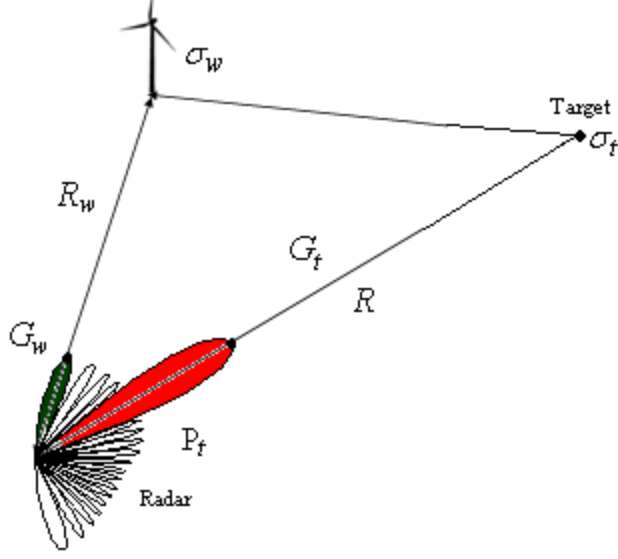
Figure 6. This geometry illustrates the monostatic case.

Normally, the signal-to-noise ratio (SNR) is used in radar and communication system performance measurements. In the case of wind turbine RCS, the signal-to-clutter ratio is used as the basis for performance evaluation. The clutter power return from a wind turbine point target with RCS σ_w at the range R_w is

$$C = \frac{P_t G_w^2 \lambda^2 \sigma_w}{(4\pi)^3 R_w^4 L} |F_w|^4 \tag{4}$$

where G_w is the antenna gain in the direction of the wind turbine and F_w is the one-way voltage path gain (propagation) factor. Note that both the target and wind turbine RCS are time-varying. For the wind turbine this is due to blade rotation and the associated change in multipath due to its rotating motion; for the target this is due to changing aspect angle, velocity and multipath. From (3) and (4) we derive the SCR for the monostatic case

$$\frac{S}{C} = \left(\frac{G_t^2}{G_w^2} \right) \left(\frac{\sigma_t}{\sigma_w} \right) \left(\frac{R_w^4}{R^4} \right) \left(\frac{|F_t|^4}{|F_w|^4} \right). \tag{5}$$

9

Note that the SCR cannot be increased by increasing the transmitter power because the clutter power increases with the target power. For a line-of-sight (LOS) condition ($|F_t| = |F_w| \approx 1$), the tradeoffs between the factors R/R_w and σ_t/σ_w in (5) are shown in Figure 7 [24]. The curves are drawn for a reference of $\mathrm{SCR}_{\mathrm{ref}} = 0\,\mathrm{dB}$. Given R/R_w, the curves provide a relative SCR by moving them on the vertical axis. In the situation where both the target and wind turbine are not in the main beam, then low sidelobes are effective in reducing interference.
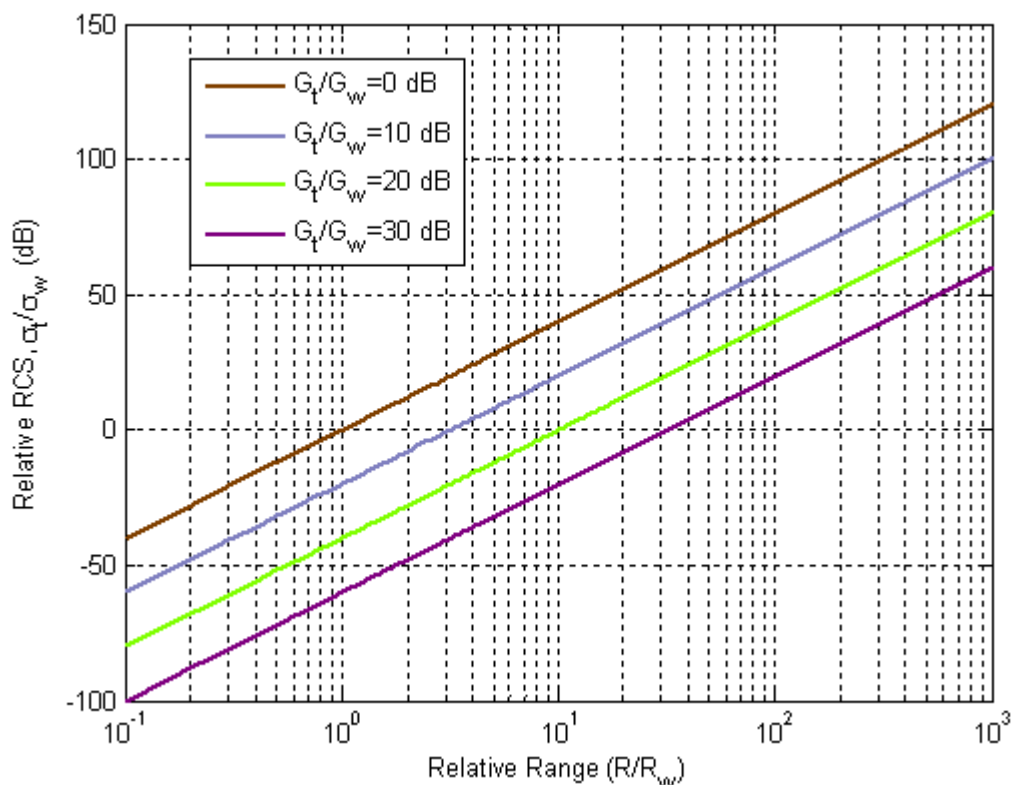
Figure 7. Universal curves show the relationship between the factors in (5).

Because of the complex propagation environment and geometry, the relative phases between the target and clutter components can be considered as random. The total power in the receiver is determined using the sum of the complex voltages V_t and V_w due to the target and clutter power returns, respectively. The subscript t denotes target, w

wind turbine. In this case, to calculate the average power, the total power received can be approximated by the sum of the target and clutter powers. If the receiver impedance is Z (real), then the total average received power is the non-coherent sum

$$P_r = \left\langle \frac{(V_t + V_w)(V_t + V_w)^*}{Z} \right\rangle = \frac{|V_t + V_w|^2}{Z} \approx \frac{|V_t|^2}{Z} + \frac{|V_w|^2}{Z} = S + C \qquad (6)$$

where $< >$ denotes expected value. This approximation allows us to consider the target and clutter components individually.

In the bistatic case, consider the scenario shown in Figure 8. The direct (line-of-sight) signal from the transmitter to the receiver is [25]

$$S = \frac{P_t G_t G_r \lambda^2}{(4\pi R)^2 L} |F_d|^2 \qquad (7)$$

where R is the direct path distance between the transmitter and receiver; G_t is the transmit antenna gain in the direction of the receiver; G_r is the receive antenna gain in the direction of the transmitter; F_d is the one-way voltage (or field) direct path propagation factor and L is the system loss factor ($L \geq 1$).
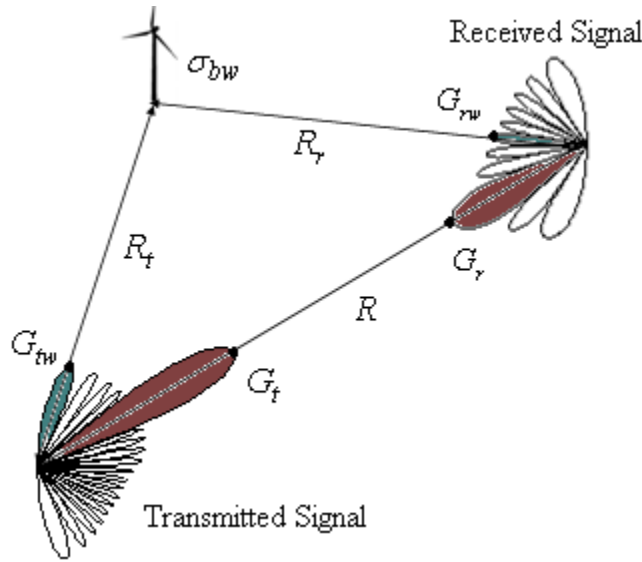
Figure 8. This geometry illustrates the bistatic case.

11

From Figure 8, the clutter power from the wind turbine arriving at the receiver is [26]

$$C = \frac{P_t G_{tw} G_{rw} \lambda^2 \sigma_{bw}}{(4\pi)^3 R_t^2 R_r^2 L_t L_r} |F_t|^2 |F_r|^2 . \tag{8}$$

The subscript w is used to denote wind turbine parameters. The subscript t refers to transmit and r to receive; σ_{bw} is the wind turbine's bistatic RCS when the incidence direction is from the transmitter and the observation direction is from the receiver, as defined in Figure 8.

For a line-of-sight propagation path and no losses ($L_t, L_r, L, |F_t|, |F_r| \approx 1$), from (7) and (8), the SCR is

$$\frac{S}{C} = \frac{G_t G_r}{G_{tw} G_{rw}} \frac{R_t^2 R_r^2}{R^2} \frac{4\pi}{\sigma_{bw}}. \tag{9}$$

In order to increase the SCR, aside from reducing the wind turbine RCS (σ_{bw}), the sidelobe levels of the two antennas should be as low as possible so the gains are lower in the direction of the wind turbine. Also, it is advantageous to operate the antenna system in a direction where the wind turbine RCS is low. In addition, one could change the radar pulse repetition frequency (PRF) to minimize radar signal returns from wind turbines. Also, because wind turbines are generally not efficient operating at low wind speeds, they could be turned off in low wind speeds. It is advantageous to operate in a condition where the target range is short and away (non line-of-sight) from the wind farms.

In summary, the definition of RCS and radar range equation were presented. The SCR was discussed for the monostatic and bistatic scenarios. Several ways to increase the SCR were addressed. Several numerical methods and software packages used to predict the RCS are presented in the next chapter.

III. RCS PREDICTION METHODS

In this chapter, a brief overview of the various methods of RCS prediction is presented. Several commercial software packages used for RCS numerical computations are discussed.

To determine the RCS of three-dimensional complex objects, such as wind turbines, we require a numerical solution of some variation of Maxwell's equations, or high frequency approximations of them, in either integral or differential form. Maxwell's equations are solved using the related boundary conditions of the problem. Rigorous methods include the method of moments (MoM) [27] or the finite difference time domain (FDTD) method [28]. The MoM obtains the solution of integral equations in the frequency domain. FDTD finds solutions of the differential equations in the time domain. The finite element method (FEM) is also used in both the time and frequency domains [29]. The Fourier transform provides a relationship between the time and frequency domain solutions.

The MoM is appealing because it is a rigorous solution that includes all the interactions between currents on the structure and, thus, all scattering mechanisms (multiple reflections, diffraction, surface waves, etc.). The MoM requires dividing or meshing the surface of the object into facets with edge lengths small compared to the wavelength. The electric and magnetic field integral equations are solved by reducing them to a matrix equation of an order approximately equal to the number of internal edges.   From this matrix equation, we solve for the current. This resulting current is used in the radiation integrals to obtain E_p^s for use in (1). At high frequencies (e.g., 10 GHz), the MoM may require a system of equations with millions of unknowns in order to converge to a solution. Therefore, for electrically large scattering objects such as an airplane or a ship, the MoM requires multi-core personal computers (PCs) with several hundred GB of memory for its intense numerical computations.

The FDTD method can also be formulated rigorously and provides approximate, yet accurate, RCS prediction of three-dimensional complex objects. It does not require the solution of a large system of equations but does require segmentation of the scattering object and surrounding volume. The incident field is introduced into the computational domain and stepped in time throughout the computational domain to find the fields at each grid location at each instant of time. Equivalence principles are used to find the far scattered fields from the equivalent currents determined from the fields on the computational boundaries. Therefore, FDTD method requires long observation times for accurate results. The Fourier transform is needed to obtain the frequency domain fields for use in (1).

The FEM method is similar to FDTD but is generally applied in the frequency domain. It is adaptable to a wide range of geometries and materials variations. It requires segmenting each part of the scattering object and surrounding volume. The incident field is introduced into the computational domain, and the wave equation is applied throughout the domain to find the equivalent currents at each grid location. Therefore, the FEM method can require a long computational time to obtain accurate results.

The approximate high frequency (HF) methods are mainly based on geometrical optics (GO) or physical optics (PO) and their edge diffraction extensions. In the case of GO, the geometrical theory of diffraction (GTD) is used. The GO technique uses ray tracing methods similar to reflection and refraction in optics to analyze electrically large targets ($\geq 10\lambda$) of arbitrary shape. The formulas are derived on the basis of infinite frequency, and the source and observation points must satisfy Snell's Law or the reflected field is zero. In the case of PO [24], the physical theory of diffraction (PTD) is used. The PO technique estimates the induced surface current on the illuminated portions of the object to be proportional to the incident magnetic field intensity and then integrates this surface current to get the scattered far-field. The current is set to zero on the shadowed portion of the target. Because of this, the computed field values at wide angles and in the shadow regions are not accurate.

Hybrid solution methods can include a mix of the PO and GO (for example, the shooting and bouncing ray (SBR) method [30]). The approximate high frequency methods require surface meshing, but the primary mesh criterion is that it adequately conforms to the actual surface. A bundle of incident rays is "shot" and traced throughout the model, including transmission through any electrically transparent material, to find reflection points, diffraction points, and shadows (due to blockage). This process is very time consuming for models that have hundreds of thousands of facets.

Many commercial software packages are available to handle RCS calculations. The major commercial software vendors for electromagnetic simulation are summarized in Table 3. Several software packages have multiple solvers that can be selected based on the object size and frequency range. For example, *High Frequency Structures Simulator* (HFSS) by Ansys has transient, frequency domain, integral equation solvers [31]. *CST Microwave Studio* [32] also has the same capability. *FEKO* [33] is another application that is capable of mixed solutions. For example, MoM, PO, GO, and edge diffraction can be applied to different portions of the object. XGtd [34] and XFDTD use ray-tracing algorithms and uniform theory of diffraction (UTD) to estimate RCS and to predict propagation for high frequency analysis. The *Lucernhammer* software package [35] has similar capabilities to a ray tracer. It applies the SBR method, PO and PTD to predict the RCS of electrically large objects. *Lucernhammer* is used for all of the simulations presented in this thesis. Note that the *Lucernhammer* software has distribution limitations. It is available only to U.S. government agencies and contractors.

Table 3.   Major commercial electromagnetic simulation software tools.

Name	Vendor	Numerical Method
High Frequency Structure Simulator (HFSS)	ANSYS	MoM, FEM, PO
Microwave Studio	CST	MoM, FEM, MLFMM, SBR
FEKO	EM Software and Systems	MoM, FEM, PO, GO, UTD
XGtd, XFDTD	REMCON	MoM, PO, GO, UTD, MEC
Lucernhammer	DELCROSS	SBR, PO, PTD

In summary, several numerical methods and software packages used to analyze RCS were presented. Depending on the size and complexity of the object, one may choose one numerical method over the others or choose a hybrid solution method to solve the RCS problem. In the next chapter, the focus is on the simulation results of horizontal axis wind turbines, the Doppler shift induced by the rotating turbine blades, and how Doppler shift affects radar performance.

IV. SIMULATION RESULTS OF HORIZONTAL AXIS WIND TURBINES

In this chapter, the wind turbine simulation setup, including horizontal axis wind turbine computer-aided design (CAD) model dimensions and mesh types are presented. The monostatic and bistatic RCS results of horizontal axis wind turbines are presented followed by analysis of the multipath and Bragg scattering issues. The effectiveness of using non-conducting materials in the turbine blades on the RCS of a horizontal axis wind turbine is also examined. Finally, comparison plots of the Doppler shift induced by the rotating turbine blades for four frequency bands (400 MHz, 900 MHz, 2.4 GHz, 5 GHz) are presented as well as its time varying RCS.

A. HORIZONTAL AXIS WIND TURBINE MODEL

Analysis of the RCS of wind turbines requires a three-dimensional (3D) geometry CAD model in the form of planar facets. The CAD model shown in Figure 9 was obtained from [36] and scaled to give dimensions in meters.

The three-blade, horizontal axis wind turbine configuration has approximately a 60 m tower height and 80 m blade diameter. These dimensions are similar to the dimensions of the commercial 1.5 MW power class of wind turbines. The dimensions for the horizontal axis wind turbine configuration are listed in Table 4.

Table 4.   The dimensions of the horizontal axis wind turbine configuration.

Three-blade horizontal axis wind turbine
Blade diameter, $D = 80$ m
Tower height, $H = 60$ m
Tower diameter at base, $d = 3.5$ m
Blade width (widest part), $w = 3.6$ m
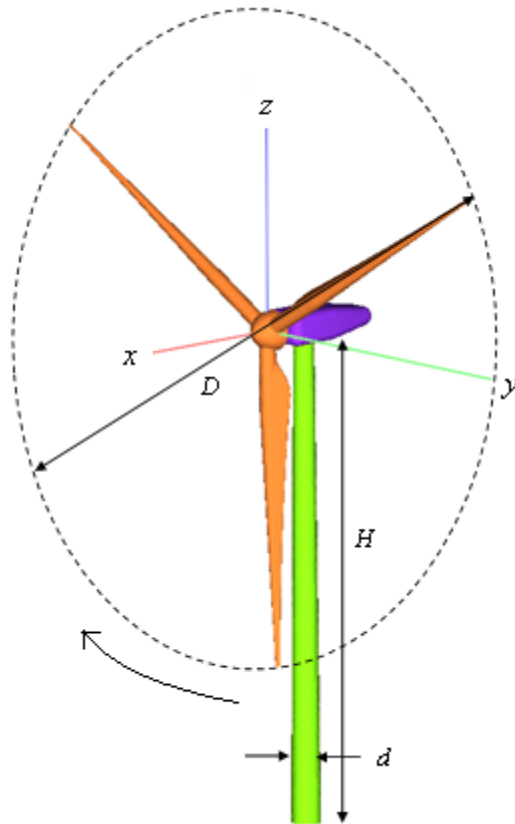
Figure 9. A horizontal axis model and its dimensions are shown. Different colors
indicate different materials used in the CAD model for simulation.

The horizontal axis wind turbine CAD model was imported by using the computer
aided-design software *ACAD* and then applying the meshing tool to generate the surface
mesh [37]. Note that the software *ACAD* has distribution limitations. It is available only
to U.S. government agencies and contractors. Both coarse and fine meshes were used in
the calculation of RCS. Examples of the wind turbine tower for coarse and fine meshes in
the CAD model are shown in Figure 10. In general, the fine mesh yields a more accurate
result in the RCS calculations but takes more time to compute the result. More discussion
of the mesh and how it affects accuracy is given in Chapter VI.

Figure 10. Different mesh types for the wind turbine tower are shown (left to right): coarse triangular (19,994 facets), fine triangular (125240 facets), and quadrilateral triangular meshes (4608 facets).

The CAD model was set up using the coordinate system defined in Figure 5 and used quadrilateral triangular meshes with a total of 37845 facets. The *x-y* plane is the ground, and the *z* axis points up. The elevation angle $(EL = \theta - 90^\circ)$ is measured from the ground. The azimuth angle $(AZ = -\phi)$ is a compass angle that is opposite to ϕ. Because the transmitter, receiver and wind turbine are at ground level, all simulation cases were set up to show only the horizontal plane patterns $(EL = 0^\circ, \theta = 90^\circ)$. The blade orientation is such that one blade is vertical and down, as shown in Figure 9. This is referred to as the 0° rotation state. Front incidence is $\phi_i = 0^\circ$; side incidence is $\phi_i = 90^\circ$.

B. SIMULATION RESULTS FOR THE HORIZONTAL AXIS WIND TURBINE RCS

As previously stated, to perform the RCS calculations, the software package *Lucernhammer* was used, which uses high frequency methods with ray tracing to compute the RCS of complex shapes. The four frequencies selected are representative of

wireless, cellular, and radar bands: 400 MHz, 900 MHz, 2400 MHz and 5 GHz. Edge diffraction was not considered in calculating the RCS. The number of rays per wavelength was set to ten. The maximum number of ray bounces was set to five. The incident wave was set to linear polarization. All surfaces of the wind turbine were set to perfect electrically conducting (PEC). The blade orientation is at $0°$ rotation state. The monostatic RCS data for the three-blade wind turbine is shown in Figure 11. The azimuth angle ϕ changes from 0 to 360 degrees, and the elevation angle is set at $\theta = 90°$.

Notice lobes occur at $90°$ and $270°$ for all four frequencies because of the large flat sides of the nacelle. Also, the RCS varies with angle as the scattering from the tower, blades, and nacelle that add and cancel with each other. As the frequency is increased, the differences in phase change more rapidly because the distances between them are longer in terms of wavelength. Thus, the RCS changes faster with angle.

The relatively high monostatic RCS in the range of $100°$ to $200°$ at 400 MHz is a result of the scattering from the tower. The diameter at the base is larger than at the top, so a wave incident at 0 degrees elevation is reflected upward such that an observer at 0 degrees elevation is in the peak of the first sidelobe. At 900 MHz the sidelobes are narrower, and an observer at 0 degrees elevation is in a null between two sidelobes. This is the reason for the large change in RCS between 400 MHz and the higher frequencies (900 MHz, 2.4 GHz and 5 GHz). Also, the periodic oscillations in the RCS in this region ($100°$ to $200°$) at 400 MHz are due to Bragg scattering from the vertical blade and tower as shown in Figure 12.

20
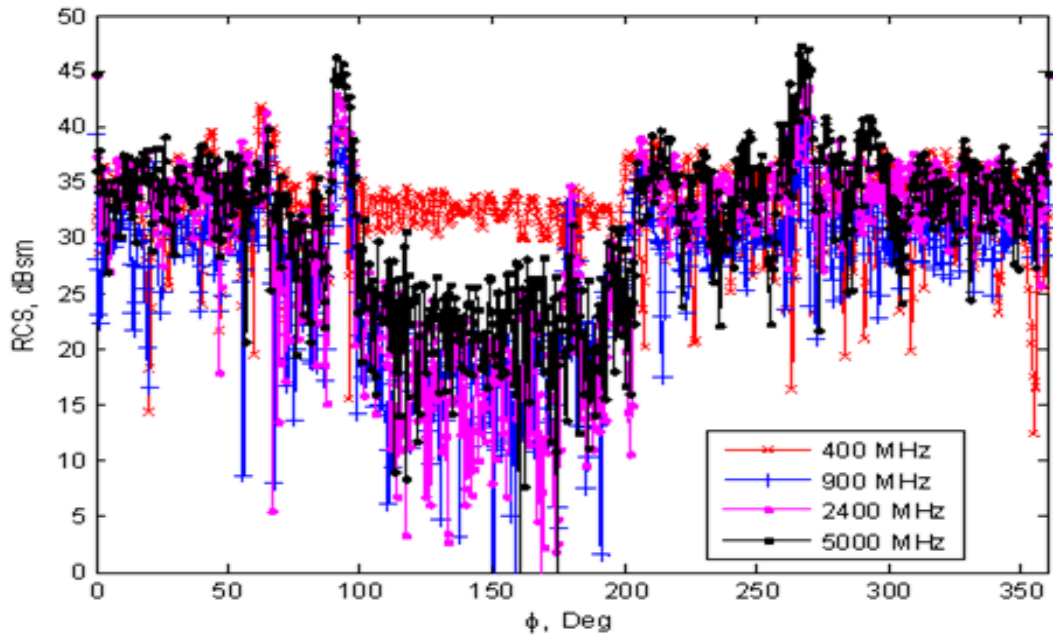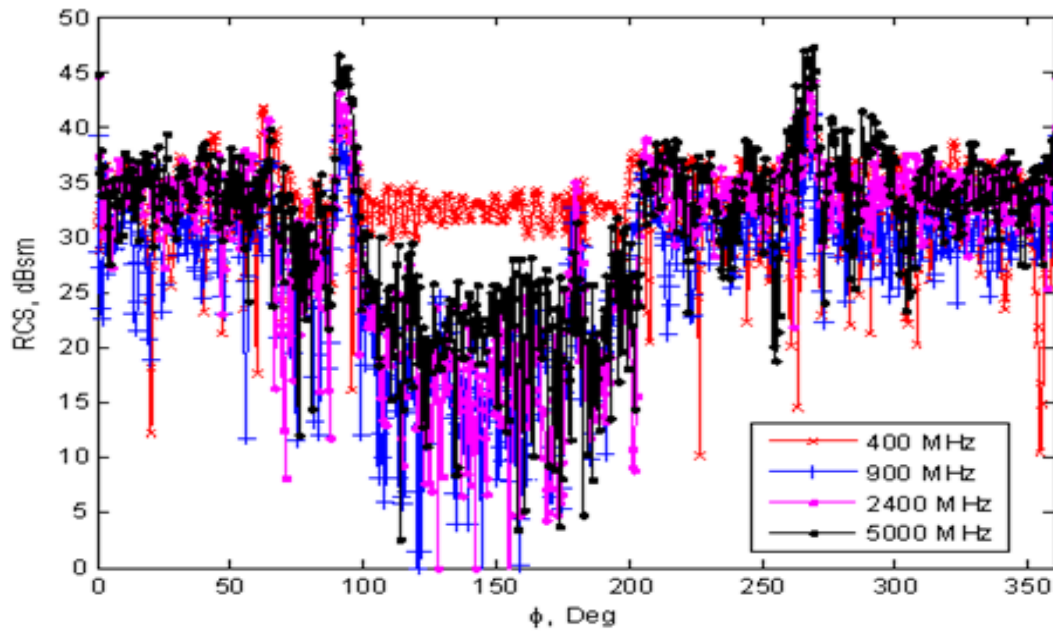
Figure 11. Comparison between four frequencies of azimuth monostatic co-polarized RCS of the horizontal axis wind turbine with all metal surfaces, $\theta = 90^{\circ}$: (a) $\sigma_{\theta\theta}$, (b) $\sigma_{\phi\phi}$.
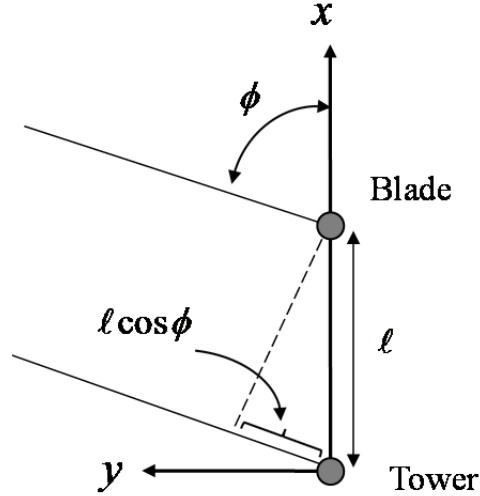
Figure 12. Illustration of Bragg scattering occurring between the tower and a vertical blade (top view).

The phase difference (round trip path) between the blade and tower is a multiple of 2π and is satisfied by the condition [21]

$$2\left(\frac{2\pi}{\lambda}\right)\ell\sin(\phi_m) = 2m\pi, \quad m = 0,\pm1,\pm2,.... \tag{10}$$

In this case, the blade length ℓ is approximately 4 m. For monostatic RCS, the first Bragg lobe occurs at $\phi = 90°$. From (10), this gives a spacing of about $4°$ between lobes near broadside ($90°$), which agrees with the plot in Figure 11. Bragg lobes are a form of aliasing.

Comparing Figure 11 to Figure 13 (PEC versus fiberglass blades), we see that both results are about the same. There are no significant differences between the PEC and non-PEC cases for the monostatic scenario. Lobes occur at $90°$ and $270°$ for all four frequencies. Also, the RCS varies with angle as the scattering from the tower, blades, and nacelle add and cancel with each other. Similarly, the relatively high monostatic RCS in the range of $100°$ to $200°$ at 400 MHz is because of the tower. Also, the periodic oscillations in the RCS in this region ($100°$ to $200°$) at 400 MHz are due to Bragg scattering from the vertical blade and tower.
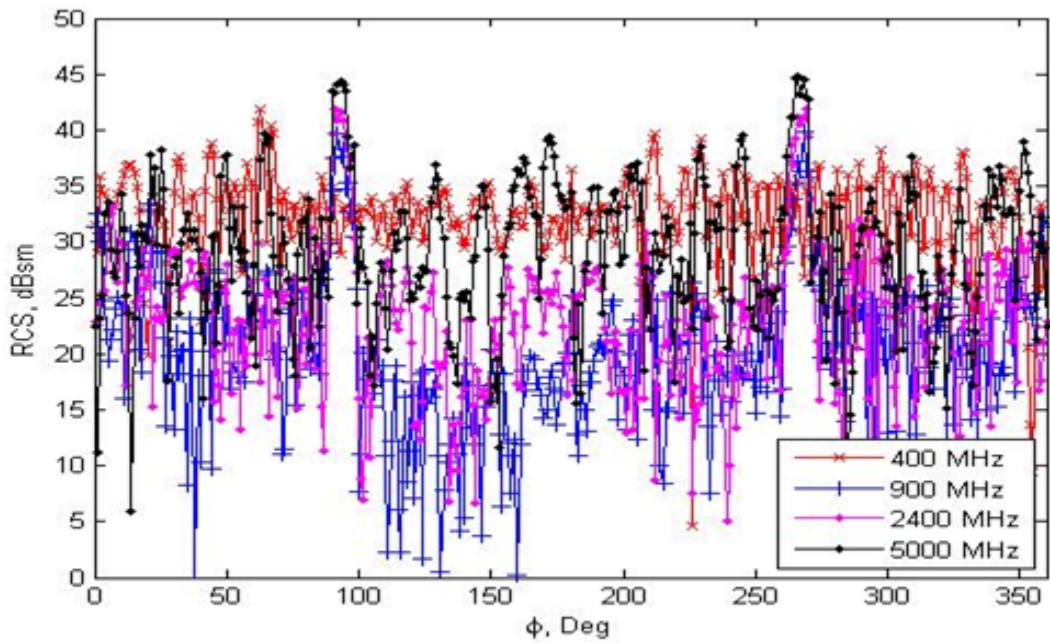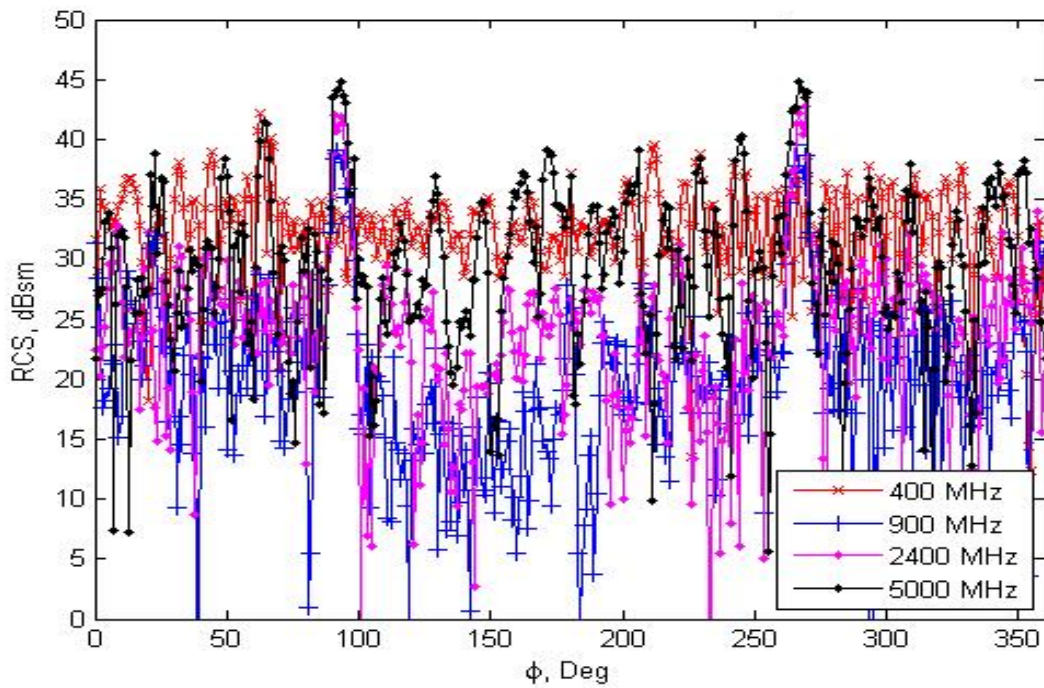
Figure 13. Comparison between four frequencies of azimuth monostatic co-polarized RCS of the horizontal axis wind turbine with fiberglass blades, $\theta = 90^{\circ}$: (a) $\sigma_{\theta\theta}$, (b) $\sigma_{\phi\phi}$.

The non-PEC case is only approximate because the *Lucernhammer* program does not trace rays transmitted through the fiberglass blades, but this contribution is negligible because the reflection loss at the air-fiberglass boundary is approximately 8 dB for a fiberglass relative permittivity of $\varepsilon_r \approx 5$ [38]. Fiberglass has an electric loss tangent $\tan \delta \approx 0.002$ [38], so in addition, there is attenuation of the transmitted wave as it propagates through the blade and a reflection loss at the other exit surface.

Bistatic patterns for the horizontal axis wind turbine with all metal surfaces, front incident ($\phi_i = 0°$) and side incident ($\phi_i = 90°$) waves are shown in Figures 14 and 15, respectively. From Figures 14 and 15, there is a clear sidelobe structure at the two frequencies of 400 MHz and 900 MHz that arises from the cylindrical tower shape. The large forward scattering lobe occurs at the observation angle $\phi = \phi_i + 180°$. This occurs at $180°$ when incidence is from the front ($\phi_i = 0°$) and at $270°$ when incidence is from the side ($\phi_i = 90°$). The forward scatter lobe increases with frequency and is orders of magnitude larger than the backscatter ($\phi = \phi_i$). This is one of the advantages that bistatic radar has over monostatic radar with regard to detecting low RCS (stealthy) targets [20]. The large lobe at $90°$ for side incidence is caused by the specular backscatter from the side of the nacelle.

Bistatic patterns for the horizontal axis wind turbine with fiberglass blades, front incident ($\phi_i = 0°$) and side incident ($\phi_i = 90°$) waves are shown in Figures 16 and 17, respectively.
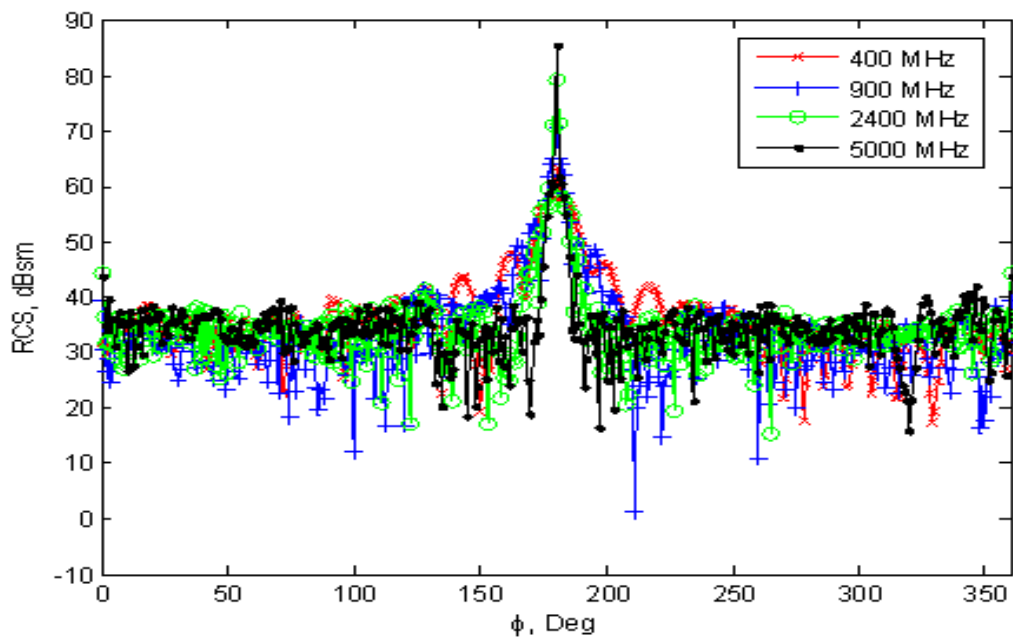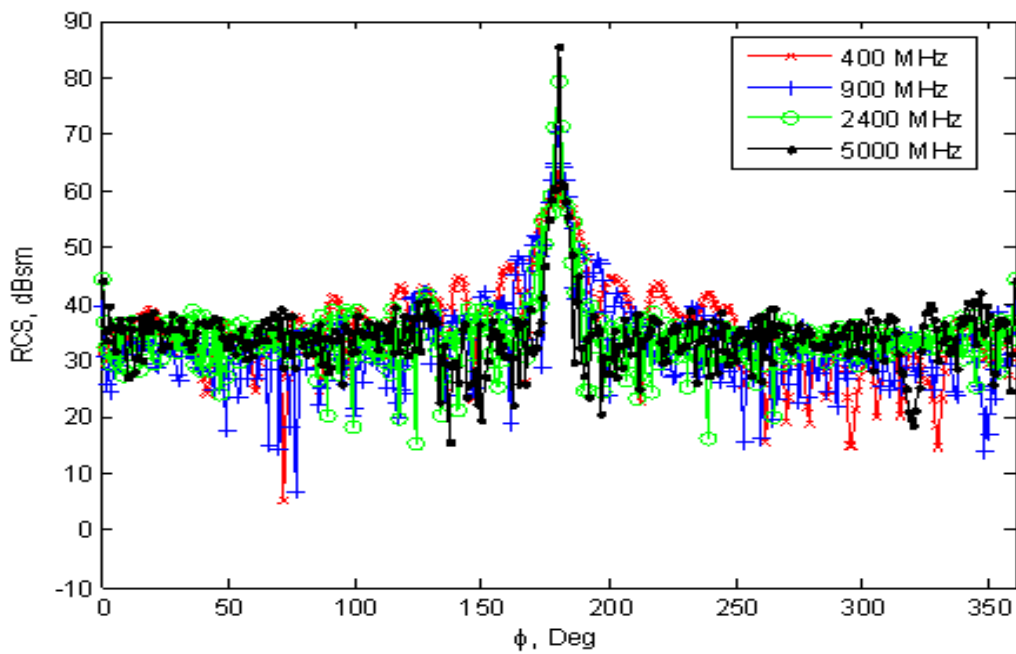
Figure 14. Comparison between four frequencies of azimuth bistatic co-polarized RCS of the horizontal axis wind turbine with all metal surfaces for an incident wave from the front ($\theta = 90^{\circ}$, $\theta_i = 90^{\circ}$, $\phi_i = 0^{\circ}$): (a) $\sigma_{\theta\theta}$, (b) $\sigma_{\phi\phi}$.
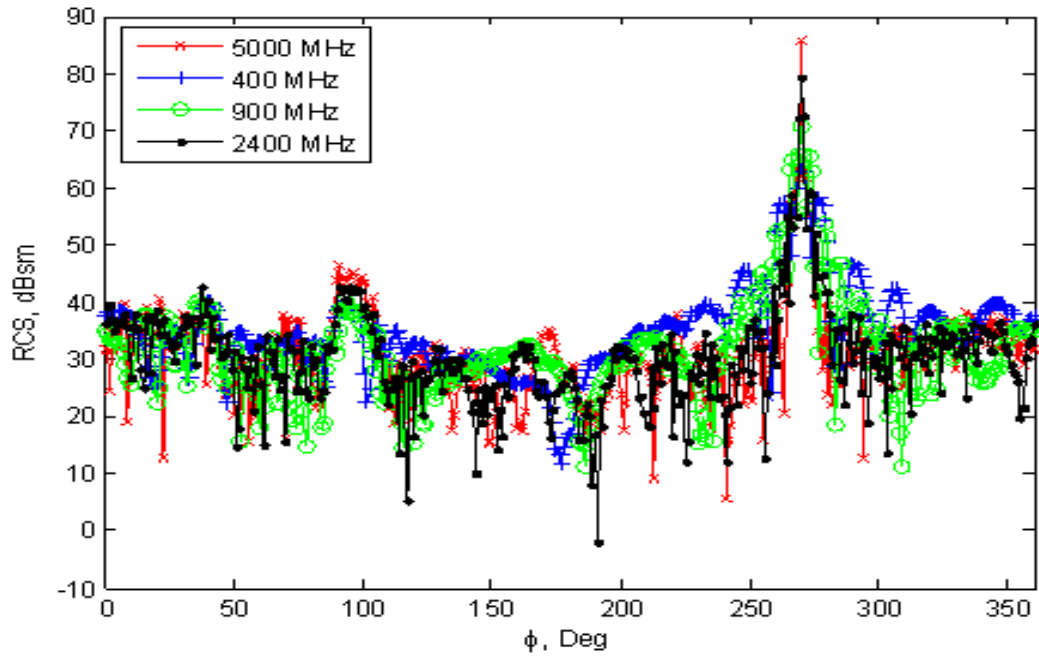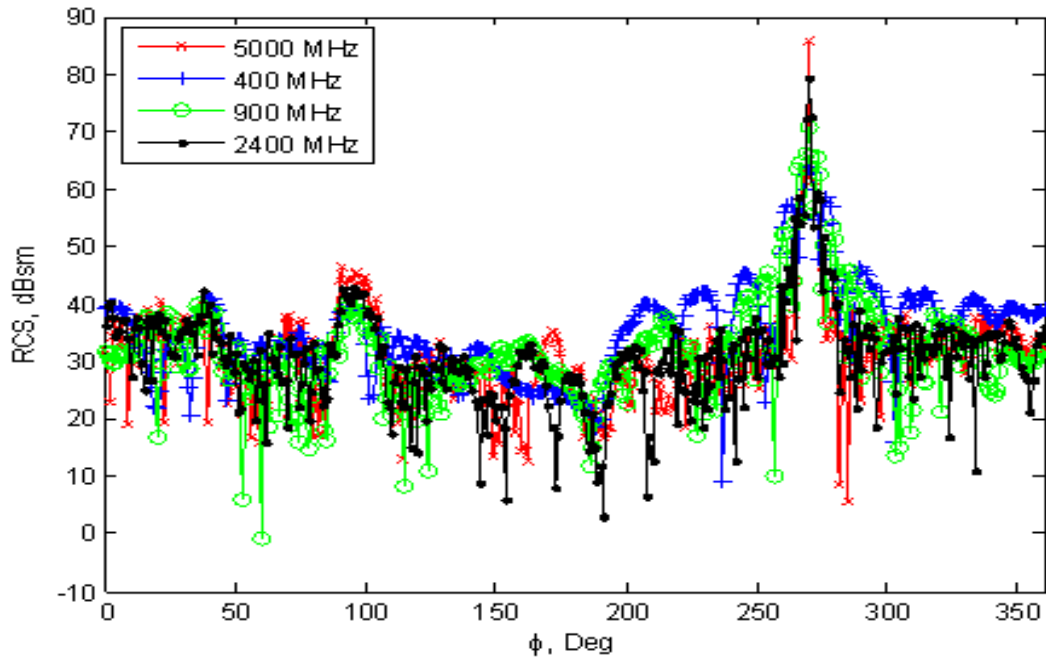
Figure 15. Comparison between four frequencies of azimuth bistatic co-polarized RCS of the horizontal axis wind turbine with all metal surfaces for an incident wave from the side ($\theta = 90^\circ$, $\theta_i = 90^\circ$, $\phi_i = 90^\circ$): (a) $\sigma_{\theta\theta}$, (b) $\sigma_{\phi\phi}$.

26
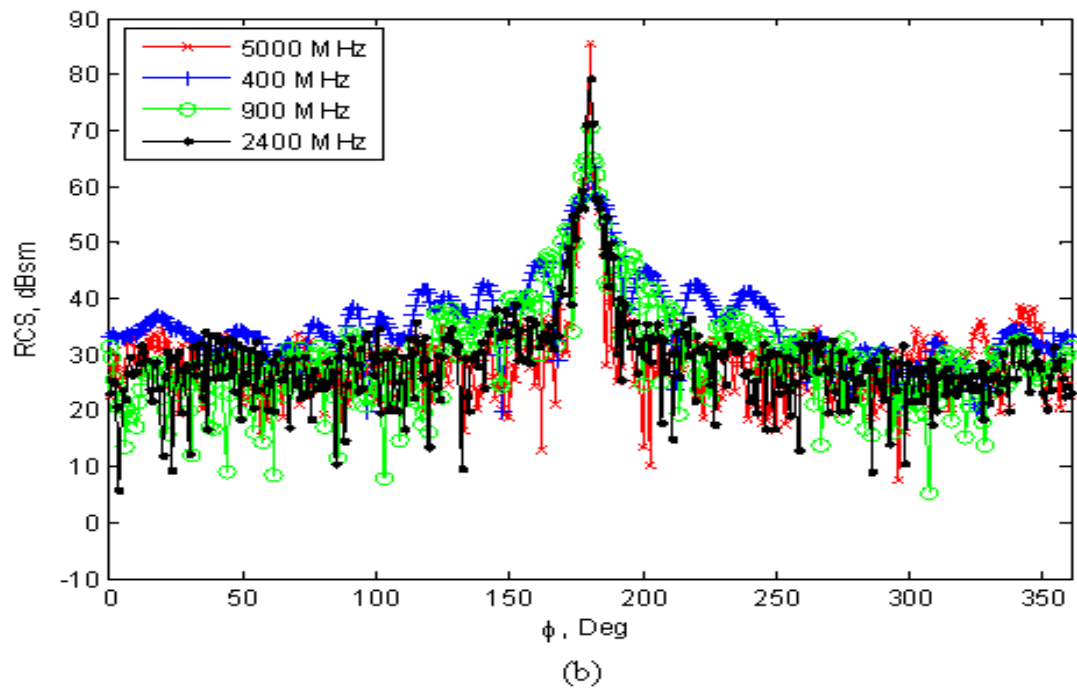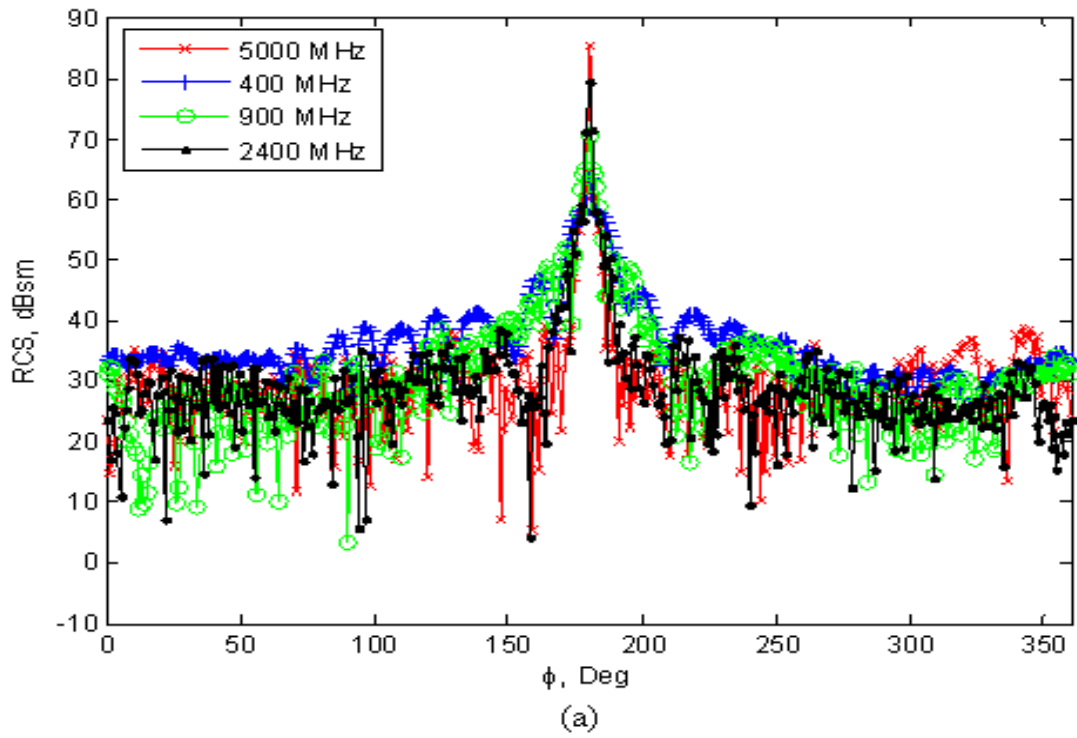
Figure 16. Comparison between four frequencies of azimuth bistatic co-polarized RCS of the horizontal axis wind turbine with fiberglass blades for an incident wave from the front ($\theta = 90^\circ$, $\theta_i = 90^\circ$, $\phi_i = 0^\circ$): (a) $\sigma_{\theta\theta}$, (b) $\sigma_{\phi\phi}$.

27
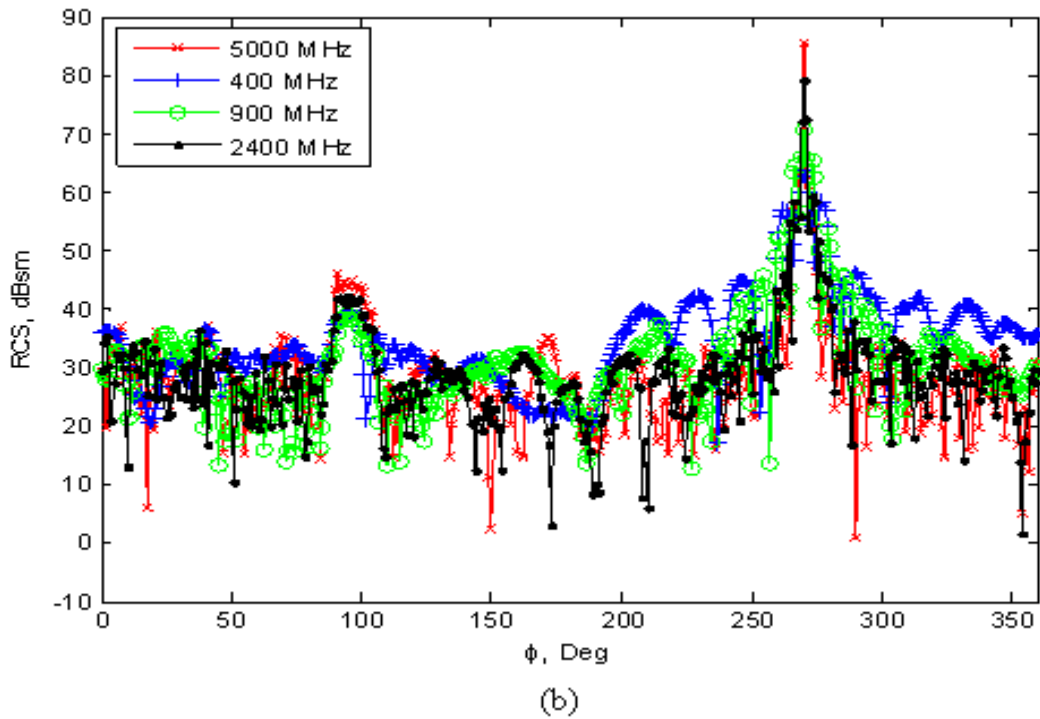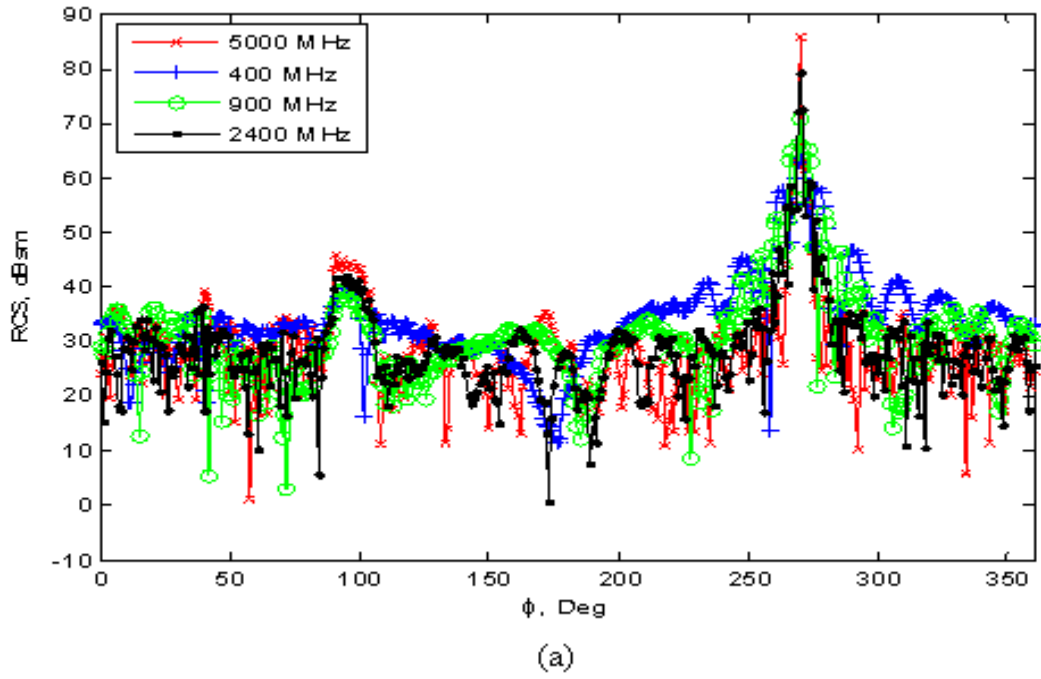
Figure 17. Comparison between four frequencies of azimuth bistatic co-polarized RCS of the horizontal axis wind turbine with fiberglass blades for an incident wave from the side ($\theta = 90^\circ$, $\theta_i = 90^\circ$, $\phi_i = 90^\circ$): (a) $\sigma_{\theta\theta}$, (b) $\sigma_{\phi\phi}$.

Comparing the fiberglass cases in Figures 16 and 17 with the PEC cases in Figures 14 and 15, we see that the effect of non-PEC blade materials (fiberglass) is not noticeable. The dominant contribution to the forward scattering is still from the tower, which is PEC in all cases. In summary, there are no significant differences between the PEC and non-PEC cases for the bistatic scenario. Generally, wire strands or a wire mesh is imbedded in the structure for grounding and lightening protection, so the conductor approximation is good at low frequencies (i.e., 400 MHz).

The individual PEC case for blade, nacelle, and tower RCS contributions are shown in Figure 18. The bistatic RCS for the nacelle, blades, and tower were computed as if each were isolated in free space. Compared to the bistatic RCS of a wind turbine at 400 MHz shown in Figure 14, each individual component of the wind turbine has a lower RCS level than the total RCS. This is expected because the sum of the scattering from the tower, blades, and nacelle add and cancel with each other but on average yield a higher RCS level. Also, the Bragg scattering from the vertical blade and tower in the 100° to 200° region at 400 MHz results in a higher RCS level.

As the wind turbine blades rotate, the bistatic RCS values vary with the rotor angles. The bistatic wind turbine RCS for rotor angles from 0° to 120° is plotted in 10° steps for the frequency of 400 MHz and is shown in Figures 19 (front incidence) and 20 (side incidence), respectively. Viewed from the front, the blade rotation is clockwise.

From Figures 19 and 20, the range of RCS values is evident, and the collected curves highlight the angular regions with the greatest variation (from 0° to 120° and from 240° to 360°). There is no significant change in the regions of the patterns at the higher RCS levels (> 40 dB), but regions with lower RCS can fluctuate 10 to 20 dB.
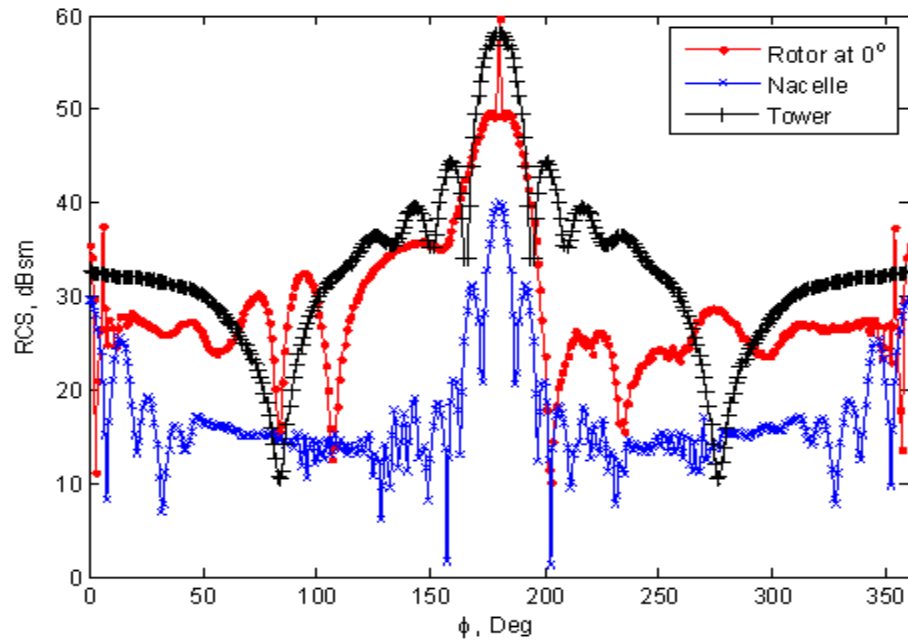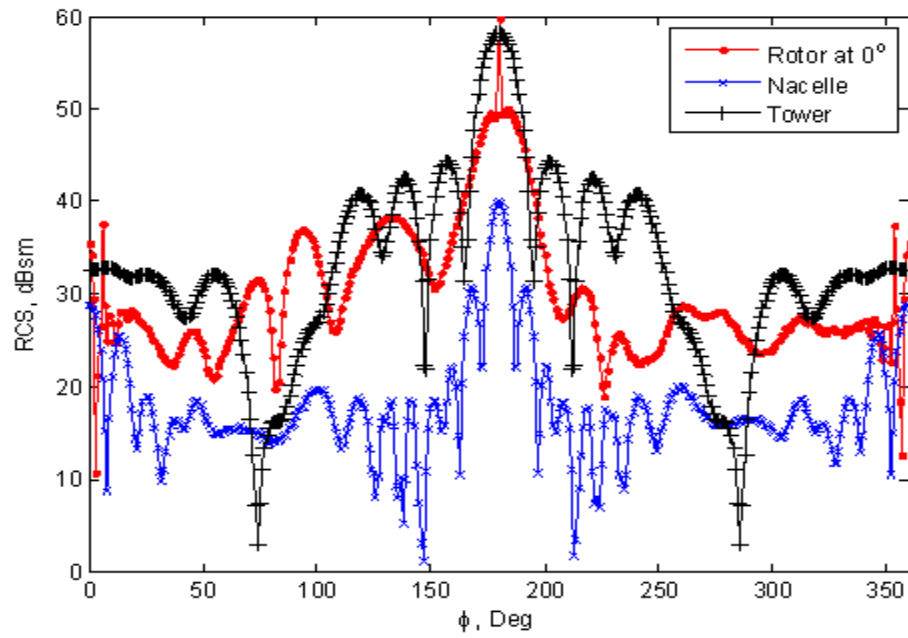
Figure 18. Comparison between the individual blade, nacelle, and tower of bistatic co-polarized RCS contributions of the horizontal axis wind turbine for an incident wave from the front ($\theta = 90^{\circ}$, $\theta_i = 90^{\circ}$, $\phi_i = 0^{\circ}$) at 400 MHz: (a) $\sigma_{\theta\theta}$, (b) $\sigma_{\phi\phi}$.
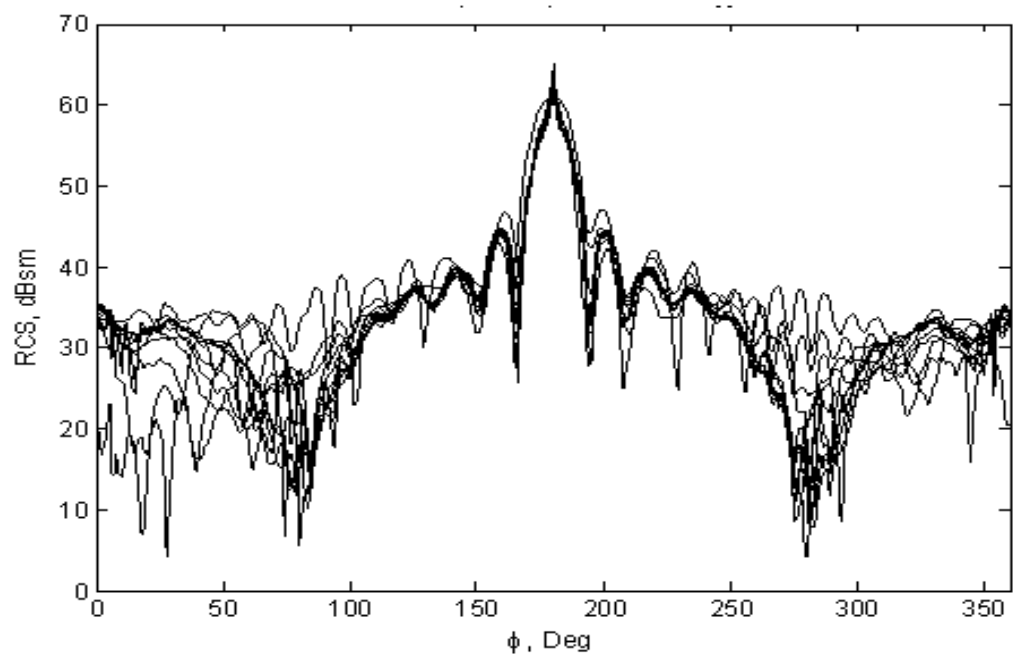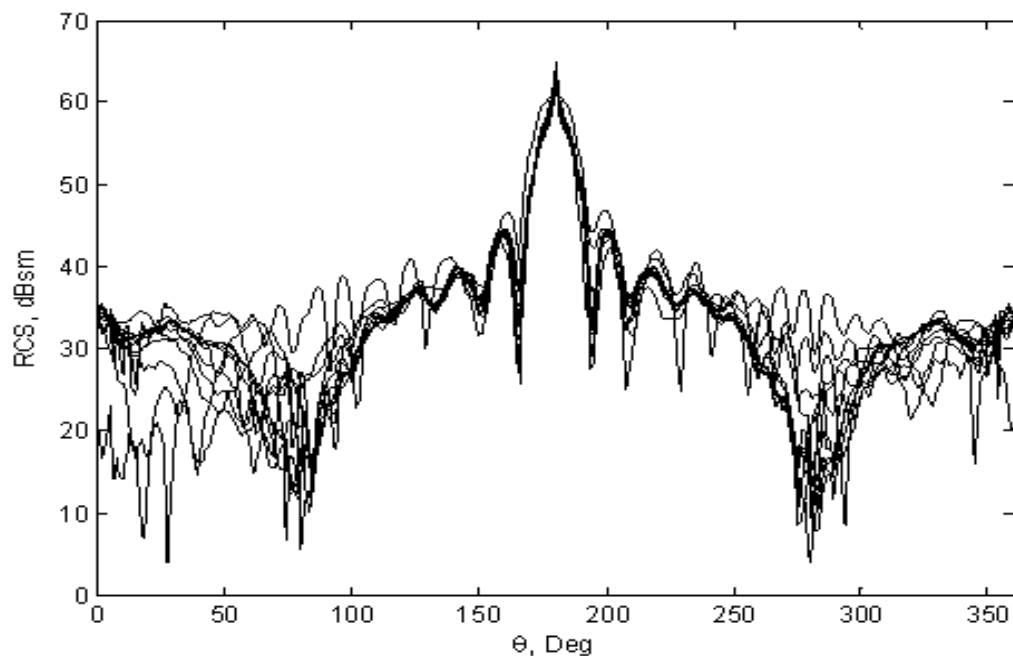
Figure 19. Azimuth bistatic co-polarized RCS for a collection of blade angles from $0°$ to $120°$ in ten degree increments, front incidence ($\theta = 90°$, $\theta_i = 90°$, $\phi_i = 0°$), fiberglass blades, 400 MHz: (a) $\sigma_{\theta\theta}$, (b) $\sigma_{\phi\phi}$.

31
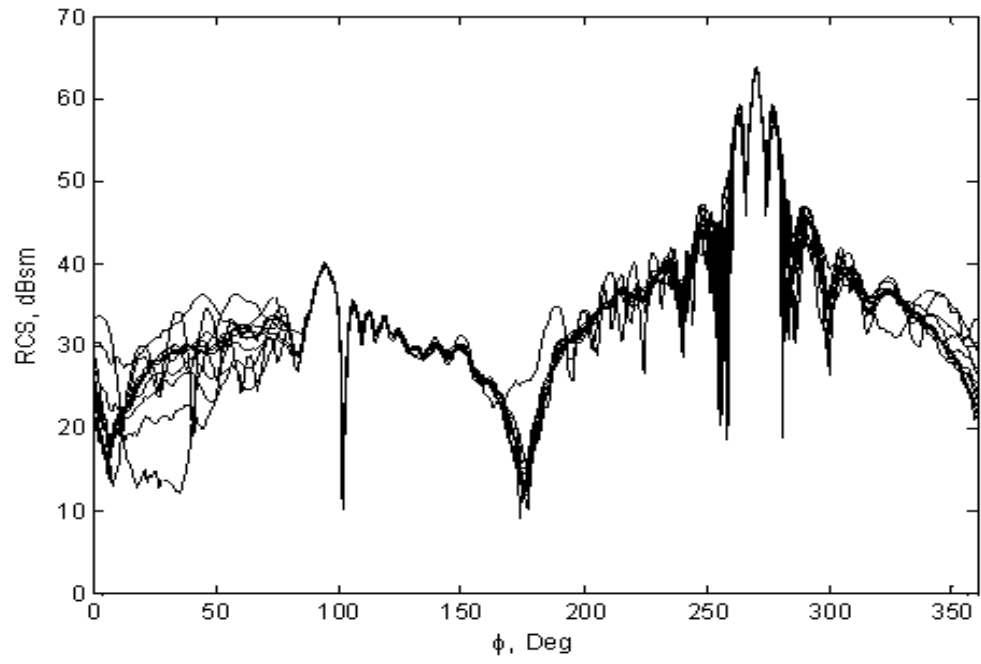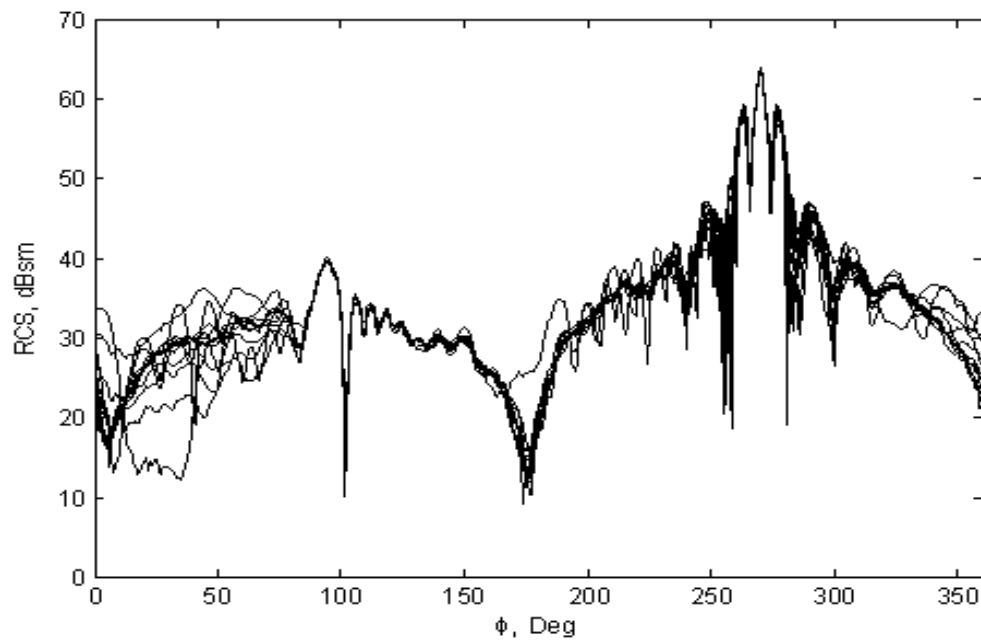
Figure 20. Azimuth bistatic co-polarized RCS for a collection of blade angles from $0°$ to $120°$ in $10°$ increments, side incidence ($\theta = 90°$, $\theta_i = 90°$, $\phi_i = 90°$), fiberglass blades, 400 MHz: (a) $\sigma_{\theta\theta}$, (b) $\sigma_{\phi\phi}$.

C. DOPPLER SHIFT FOR THE HORIZONTAL AXIS WIND TURBINE

A typical commercial 1.5 MW power class of wind turbines has a rotation rate of 15.7 revolutions per minutes (rpm) [1]. Therefore, the rotation frequency f_w is 0.2616 revolutions per second (1.644 radians per second). The length of blade r is 40 m (Table 1). The blade rotation creates time-varying Doppler spectra which can interfere with radar communication system performance. To study this Doppler effect, consider a radar signal located in the direction of the unit vector $\hat{r}_{radar}$ from the rotor with linear velocity v as shown in Figure 21. The relative radial velocity is $v_r = \vec{v} \cdot \hat{r}_{radar}$, and the Doppler shift in Hz is [23]

$$f_d = \frac{2}{\lambda} \vec{v} \cdot \hat{r}_{radar} = \frac{2\omega r \cos\theta}{\lambda} = \frac{2\omega r \cos\omega t}{\lambda}. \tag{11}$$
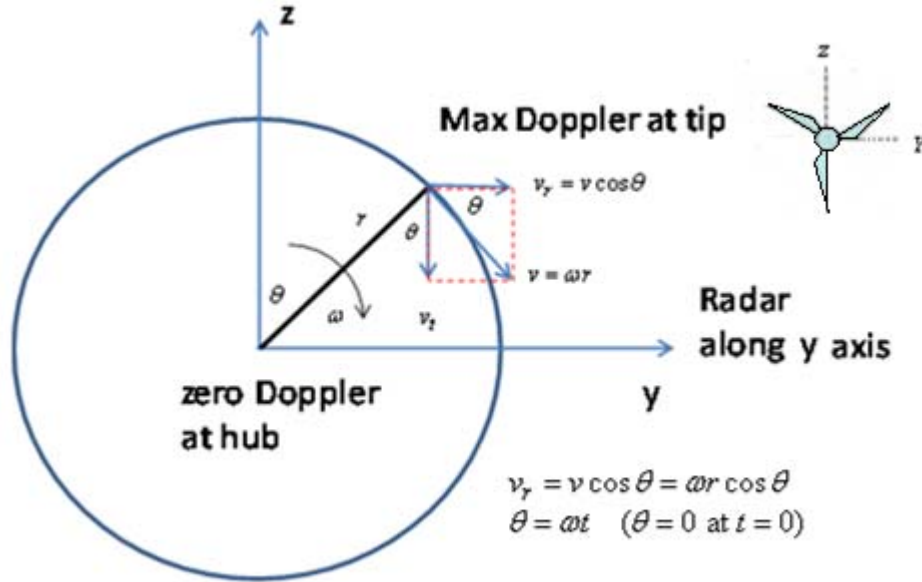
Figure 21. This geometry shows the rotation direction of the blade of length r. The radar is located along the y-axis. The peak Doppler shift occurs at the tip of the blade.

Pulse Doppler radar processing is generally done after down conversion. If direct down conversion is used, the baseband signal contains Doppler. If we are interested in measuring the Doppler, according to the Nyquist criterion the required minimum sampling frequency f_s is twice the maximum Doppler frequency ($2f_{dmax}$). For an observer

viewing from the side, the Doppler frequency is zero at the hub and changes for scattering contributions along the rotor. From (11) the maximum is

$$f_{d\max} = |\, 2v_{\max} / \lambda \,|. \tag{12}$$

The maximum velocity of the blade occurs at the tip when the blade is vertical is

$$v_{\max} = 2\pi r f_w. \tag{13}$$

Combining (12) and (13), we get the maximum Doppler frequency at the tip of the blade as

$$f_{d\max} = |\, 4\pi r f_w / \lambda \,|. \tag{14}$$

The maximum Doppler frequency and the minimum sampling frequency for the four frequencies of interest are summarized in Table 5.

Table 5.   The maximum Doppler frequency and minimum sampling frequency of the horizontal axis wind turbine RCS.

Radar frequency band	Maximum Doppler frequency $f_{d\max}$ (Hz)	Minimum sample frequency f_s (Hz)
400 MHz	175.37	350.74
900 MHz	394.63	789.26
2.4 GHz	1052.35	2104.7
5.0 GHz	2192.41	4384.82

Referring to Figure 21, we see that only the blades are contributing to the Doppler shift. The blades only contribute about half of the total RCS depending on the angles of incidence/observation. The range of Doppler frequency shift for a single blade is from 0 (at the hub) to a maximum value at the tip of the blade. As shown in Figure 22, the Doppler frequency changes, reaches maximum as the blade rotates toward the radar, and then decreases as the blade rotates away from the radar. The Doppler frequency can be plotted as a function of time for one revolution (360°) as shown in Figure 23. The maximum Doppler frequency for each of the frequency bands in both Figures 22 and 23 is in agreement with Table 5.

34
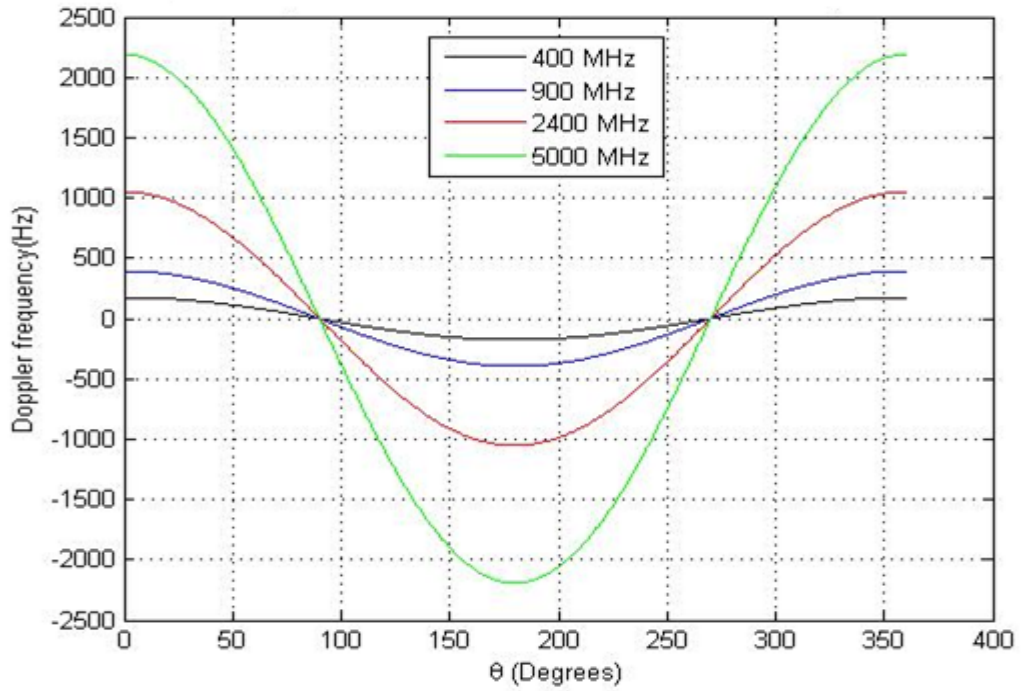
Figure 22. Blade length $r = 40$ m; θ measured from the vertical blade position. The Doppler shift of a blade as it is rotated one revolution.
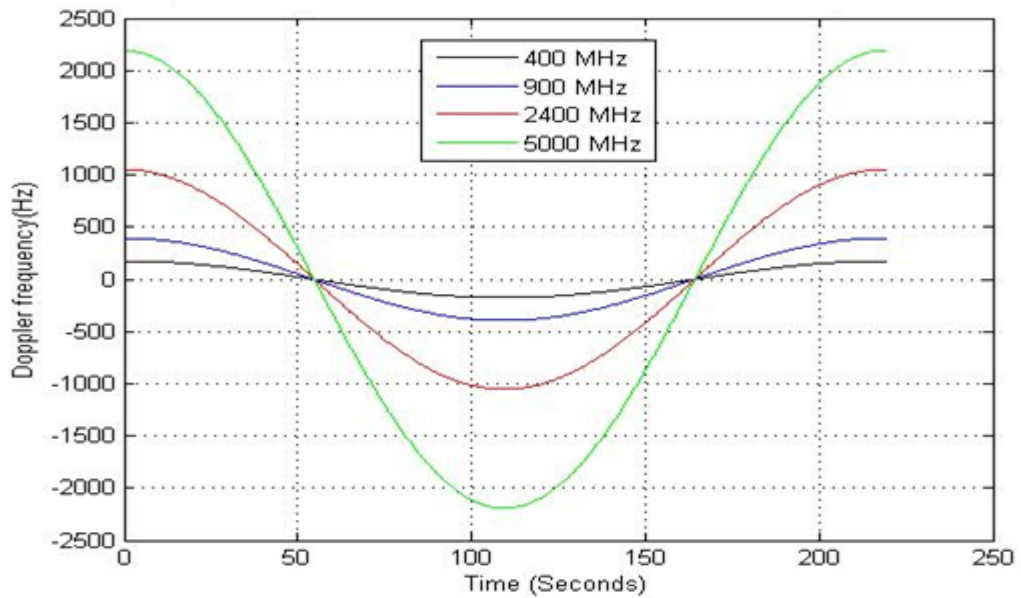
Figure 23. Doppler frequency as a function of time as the blade is rotated one revolution at 15.7 rpm. Blade length $r = 40$ m; $t = 0$ measured at the vertical blade position.

35

In the monostatic far-field analysis ($R \gg r$), the blade cross-section can be considered approximately constant from the hub to the tip. If the blade cross-section were constant along the length, each differential length of the blade would contribute equally to the total RCS as shown in Figure 24. Each length $d\ell$ would contribute $d\sigma$ to the total RCS. Because the distance $R \gg r$, the difference in range between the segments and the radar is negligible for the $1/R^2$ term in the radar equation. The scattered power spectrum should be almost uniform over the baseband frequencies from $-f_{d\text{max}} \leq f_d \leq f_{d\text{max}}$.
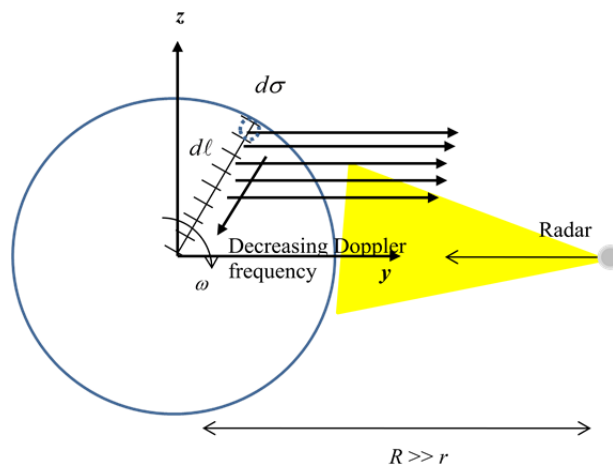
Figure 24. This geometry illustrates how each incremental length $d\ell$ would contribute $d\sigma$ to the total RCS observed by the radar at distance R.

As the wind turbine blades rotate, the monostatic RCS values vary with the rotor angles. The monostatic wind turbine RCS for a fixed angle is plotted for rotor angles from $0°$ to $360°$ in $1°$ steps for each of the frequency bands and shown in Figures 25 (front) and 26 (side), respectively. Viewed from the front, the blade is at the vertical position ($\theta = 0°$) and rotating clockwise. Note that from the front there is no Doppler shift because the blades are rotating in a plane perpendicular to the radar LOS. As illustrated in Figures 27 and 28, the range of RCS values is evident, and the collected curves highlight the angular regions with the greatest variation (from $60°$ to $175°$ and from $240°$ to $360°$).
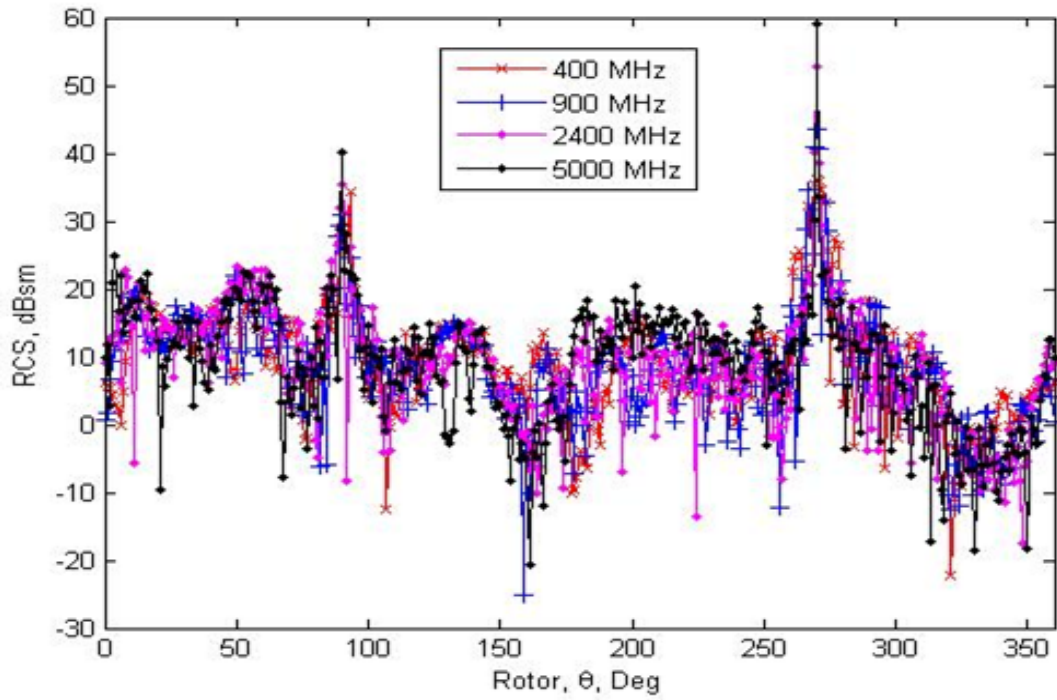
(a)
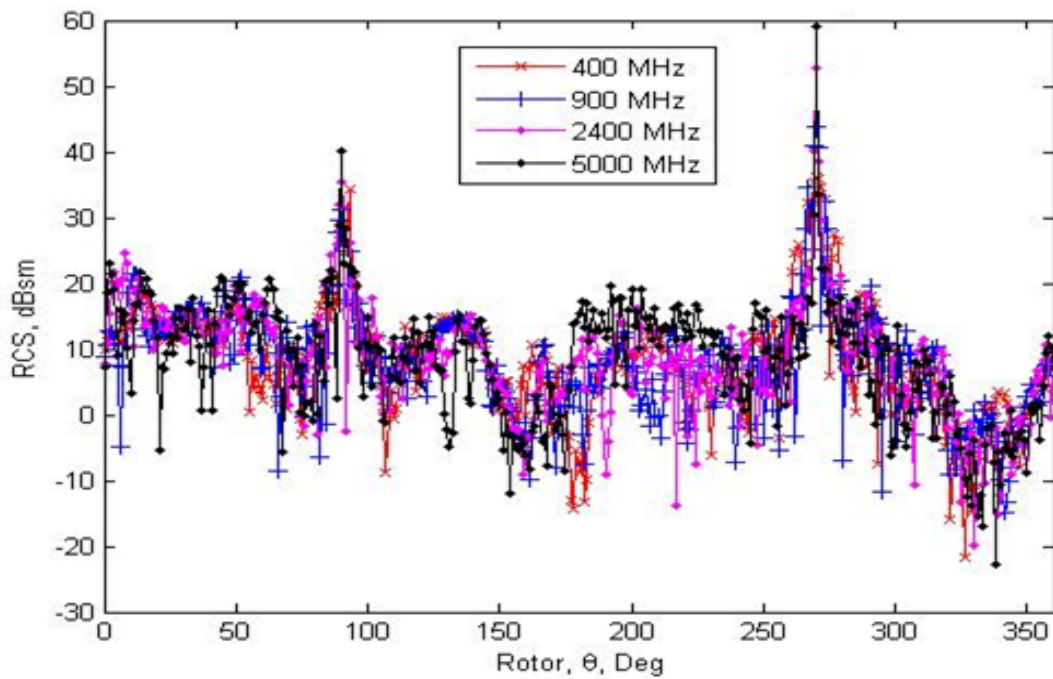
(b)

Figure 25. Monstatic RCS as the blade rotates, PEC, front incidence ($\theta = 90°$, $\phi = 0°$): (a) $\sigma_{\theta\theta}$, (b) $\sigma_{\phi\phi}$.

37
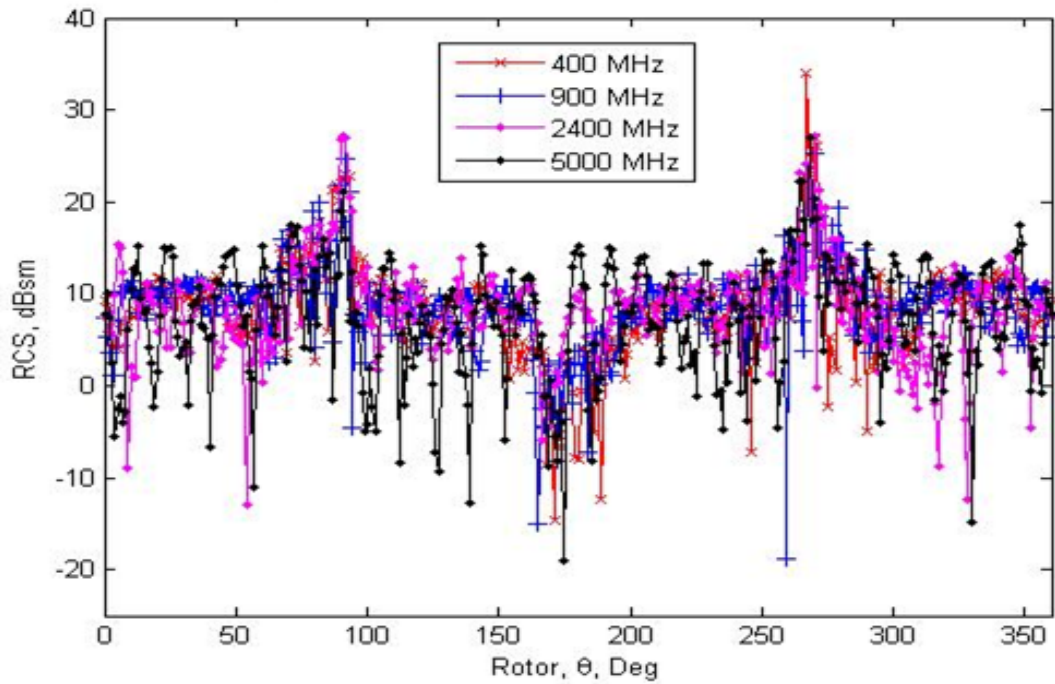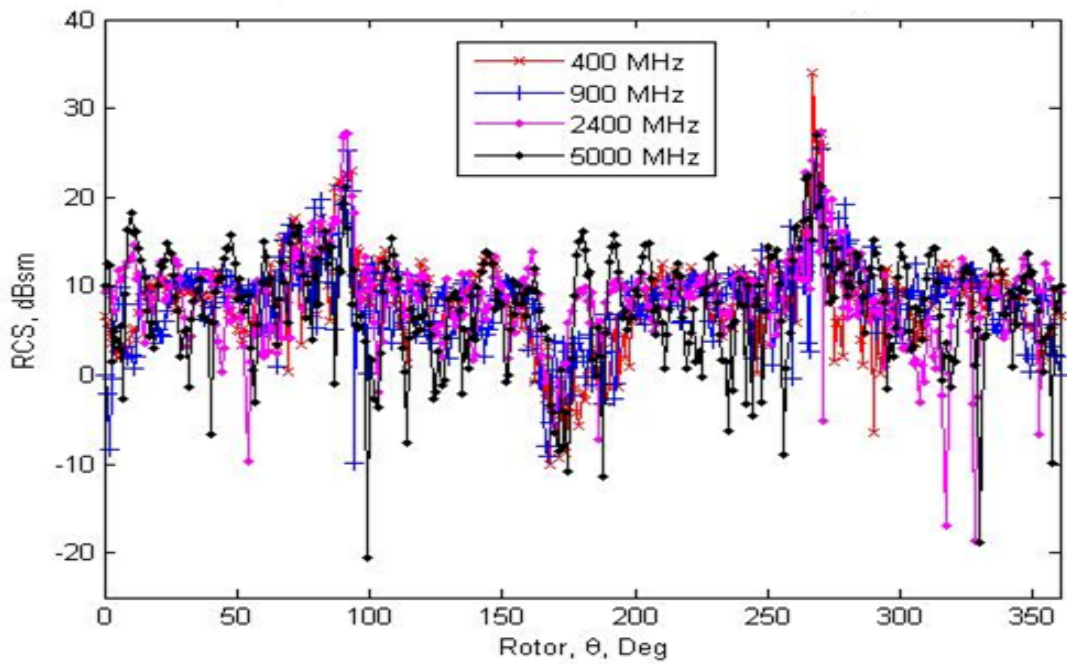
Figure 26. Monstatic RCS as the blade rotates, PEC, side incidence ($\theta = 90^{\circ}$, $\phi = 90^{\circ}$): (a) $\sigma_{\theta\theta}$, (b) $\sigma_{\phi\phi}$.
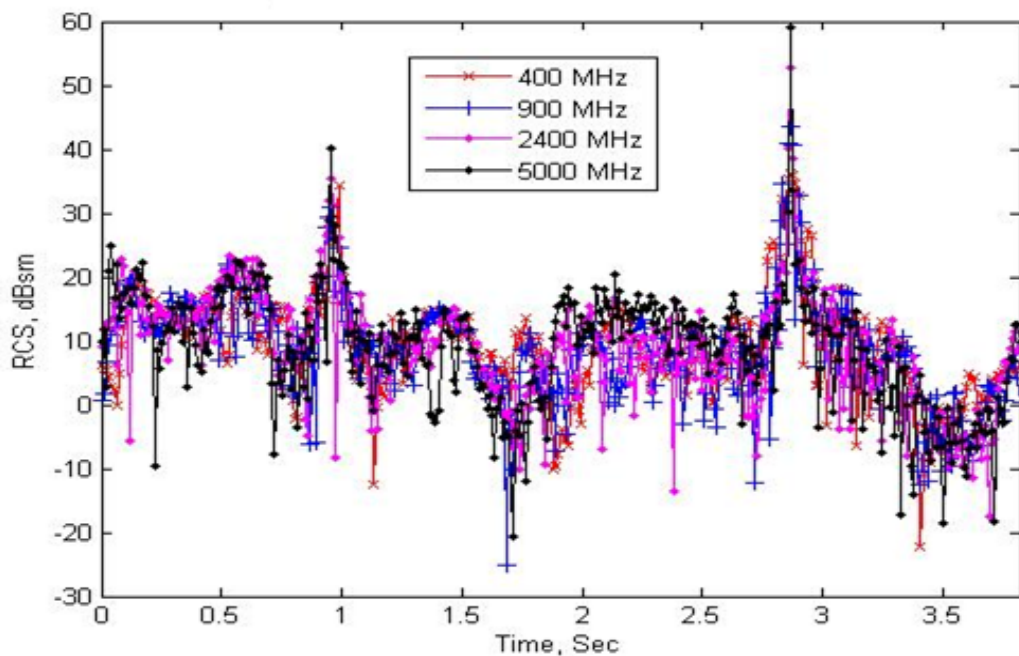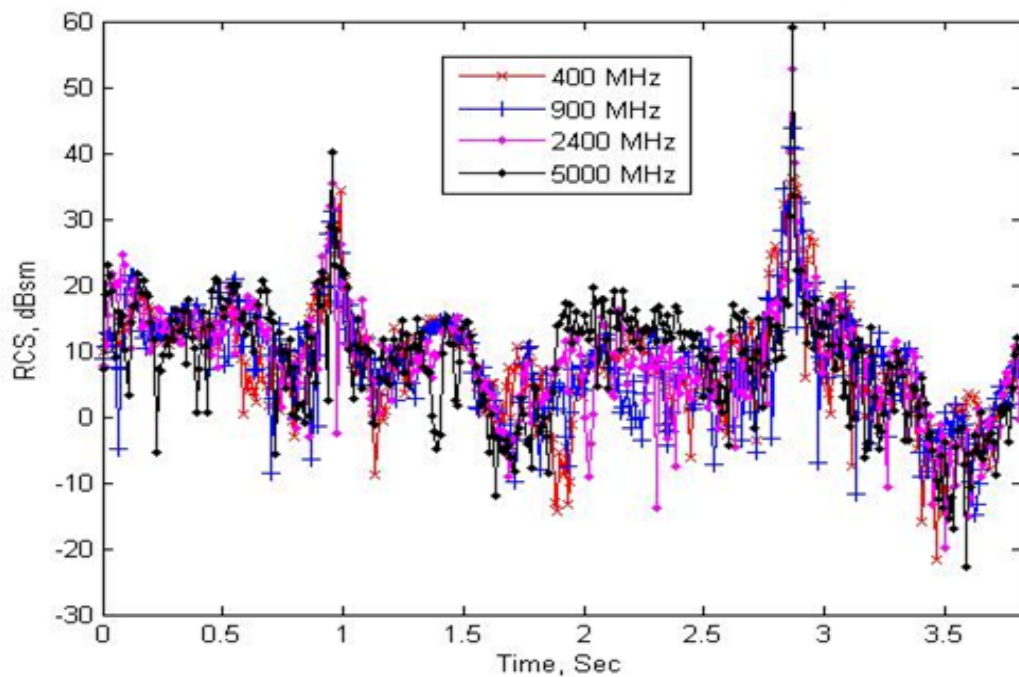
Figure 27. Computed monostatic RCS for the 80-m diameter rotor as a function of time. The plotted time represents one rotation (3.82 seconds) from the reference position at time zero (one blade at vertical), front incidence ($\theta = 90°$, $\phi = 0°$), PEC: (a) $\sigma_{\theta\theta}$, (b) $\sigma_{\phi\phi}$.

39
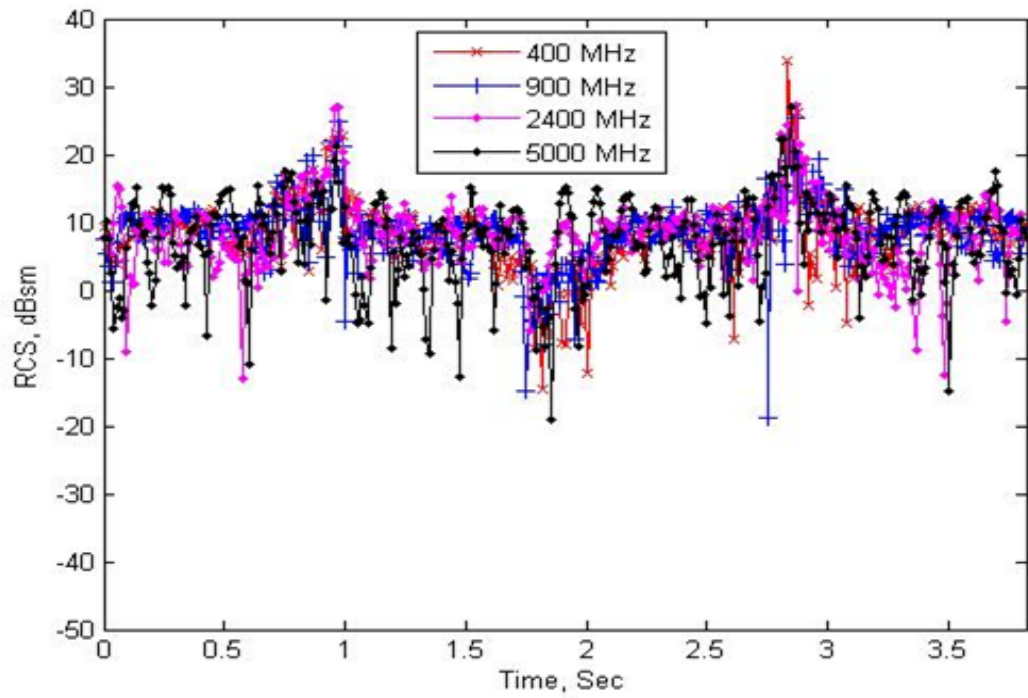
(a)
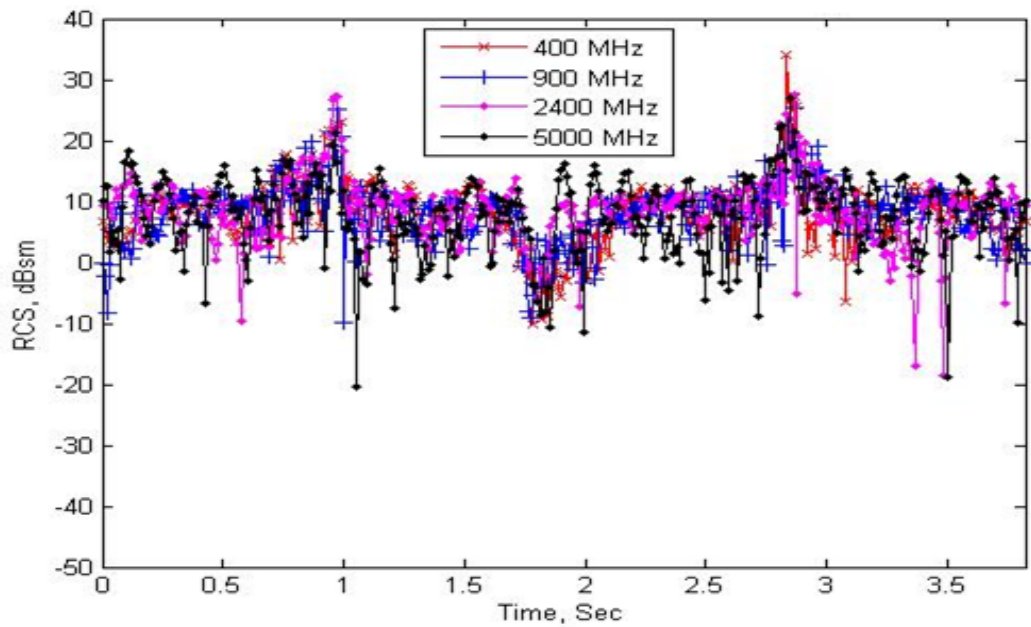
(b)

Figure 28. Computed monostatic RCS as a function of time. The plotted time represents one rotation (3.82 seconds) from the reference position at time zero (one blade at vertical), side incidence ($\theta = 90°$, $\phi = 90°$), PEC: (a) $\sigma_{\theta\theta}$, (b) $\sigma_{\phi\phi}$.

In general, the total signal received from the target and wind turbine can be expressed as

$$E_r \sim A_w \cos\left[\left(\omega_c + \omega_{dw}\right)t + \Phi_w\right] + A_t \cos\left[\left(\omega_c + \omega_{dt}\right)t + \Phi_t\right] \qquad (15)$$

where $\omega_c = 2\pi f_c$ and f_c is the carrier frequency. The subscript w refers to wind turbine and t to target. The radian Doppler shifts of the target and wind turbine are ω_{dt} and ω_{dw}, respectively. The amplitude factors A_t and A_w are a function of the range, antenna gain and RCS of the target or wind turbine. Similarly, the phase shifts Φ_t and Φ_w are due to the range delays and transmit and receive channel phase shifts. The propagation channels will also influence both A and Φ. These two signals will mix in the receive channel down conversion process. The ideal situation is when the target signal is strong compared to the wind turbine signal, and the second term dominates (large RCS or close range). If not, the mixing results in phase and amplitude errors that degrade the signal processing. The final baseband output behavior can vary depending on the receiver architecture and applied filtering.

In phase coherent systems, the phase error introduced by the Doppler shift over the extent of the observation or integration time can be used as an indicator of its impact on the processing gain. The Doppler shift required for a 2π phase shift over an observation time T is

$$\omega_d T = 2\pi \quad \rightarrow \quad f_d = 1/T. \qquad (16)$$

For example, consider a long range ultra-high frequency (UHF) 400 MHz search radar with a pulse width $\tau = 60$ μs and a pulse repetition frequency of 300 Hz as depicted in Figure 29. The Doppler shift that gives a 2π phase shift across a pulse width is 16.67 kHz (1/60 μs), which is much larger than that of a wind turbine (175.37 Hz from Table 5). However, if 60 pulses are integrated, the time on target is

$$\frac{60 \text{ pulses}}{300 \text{ pulses/sec}} = 0.2 \text{ sec}. \qquad (17)$$

41

A Doppler shift of 5 Hz (1/0.2 seconds) gives a 2π phase shift over this interval. The Doppler shift will not corrupt the phase over a pulse width, but it can limit the number of pulses that can be integrated efficiently.
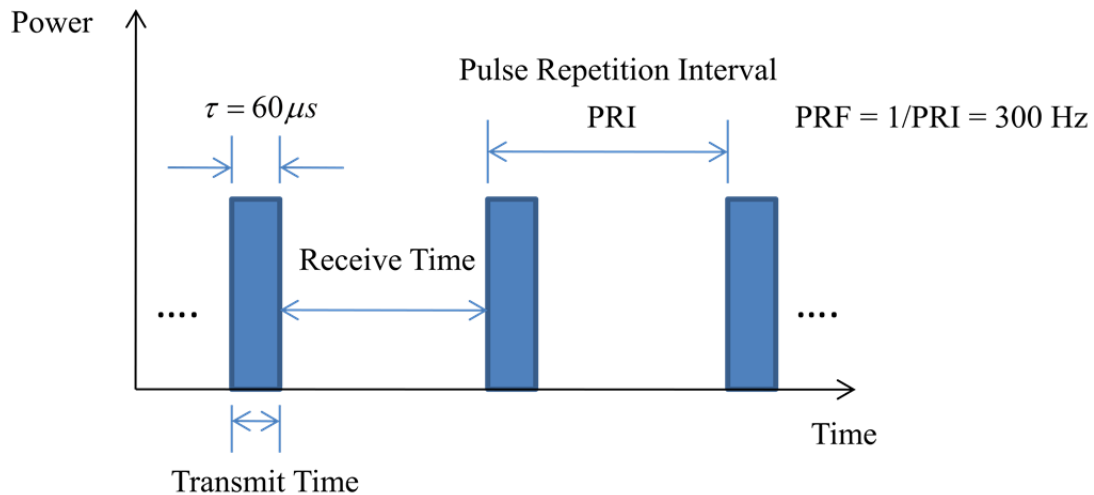
Figure 29. Example of long range UHF search radar pulsed waveform.

In moving target indication (MTI), clutter cancellers are often used to suppress clutter and improve the SCR. A filter that has a notch at the Doppler frequency of the clutter is used to reduce the clutter power. If the wind turbine Doppler shift is almost the same as that of the "normal" clutter that the filter is designed to cancel (foliage wind motion, weather, etc.), then the wind turbine clutter will be rejected. Given but the wide range of operating scenarios this is unlikely.

Doppler shift is an important measurement parameter in modern radars. Measurements of its characteristics are used to suppress clutter and to identify targets with moving components (e.g., wind turbines, helicopters). In general, a low PRF system (100 Hz to 4 kHz) is unambiguous in range. The unambiguous range is the maximum distance from the range to a target that the radar can measure unambiguously. On the other hand, a high PRF system (10 kHz to 100 kHz) is unambiguous in Doppler shift. This means the Nyquist sampling criterion is satisfied for the fastest target of interest. In

between these two conditions is the medium PRF system (8 kHz to 30 kHz), which is unambiguous in both range and Doppler.

In summary, the wind turbine simulation setup, including horizontal axis wind turbine CAD model dimensions and mesh types were presented in this chapter. In general, the fine mesh yields a more accurate result in the RCS calculations but takes more time to compute the result. The monostatic and bistatic RCS results of horizontal axis wind turbines were presented, followed by an analysis of multipath and Bragg scattering issues. There are no significant differences in RCS between the PEC and non-PEC cases for the monostatic and bistatic scenario. The motion from the rotating turbine blades and its large time varying RCS cause a Doppler shift that can interfere with the receiver processing.

The simulation results and advantages of vertical axis helical wind turbines are discussed in the next chapter.

THIS PAGE INTENTIONALLY LEFT BLANK

V. SIMULATION RESULTS OF VERTICAL AXIS WIND TURBINES

In this chapter, the advantages of the vertical axis helical wind turbine design are discussed. The wind turbine simulation setup, including vertical axis wind turbine CAD model dimensions, is presented. The monostatic and bistatic RCS patterns of vertical axis wind turbines are presented for the four frequencies (400 MHz, 900 MHz, 2.4 GHz and 5 GHz) followed by an analysis of the multipath and Bragg scattering issues. The effect of using non-conducting materials in the turbine blades on the RCS of a vertical axis wind turbine is also discussed.

A. VERTICAL AXIS WIND TURBINE MODEL

Since the early 1900s, many vertical axis wind turbines have been developed and used commercially. Many have a helical blade design and, because of their compact size and low cost, have been proposed as urban rooftop energy solutions [39]. The helical wind turbine is quieter than bladed wind turbines because of slower speed along the blade tips. Helical wind turbines can be tower mounted or mounted close to the base. The advantage of the helical wind turbine design is that it can operate in slow wind speeds (11 miles per hour). Another advantage of the helical wind turbine is that it can be used in areas with higher wind speeds (75 miles per hour) where bladed wind turbines are unsafe to operate. Also, helical wind turbines generally have less environmental concerns such as killing birds, especially in migratory paths. Helical wind turbines have fewer problems with crosswinds than bladed turbines and they do not need a tail-fan to keep them pointed in the optimal direction.

The vertical axis helical wind turbine CAD model is shown in Figure 30 with the blades in the 0° position (one bottom blade centered on the *x-axis*). Front incidence is $\phi_i = 0^{\circ}$, and side incidence is $\phi_i = 90^{\circ}$. Dimensions for the vertical axis helical configuration are listed in Table 6. These dimensions are similar to the dimensions of the commercial 6.5 kW power class of helical wind turbines. The vertical axis helical wind turbine model uses quadrilateral triangular meshes and has a total of 7059 facets.
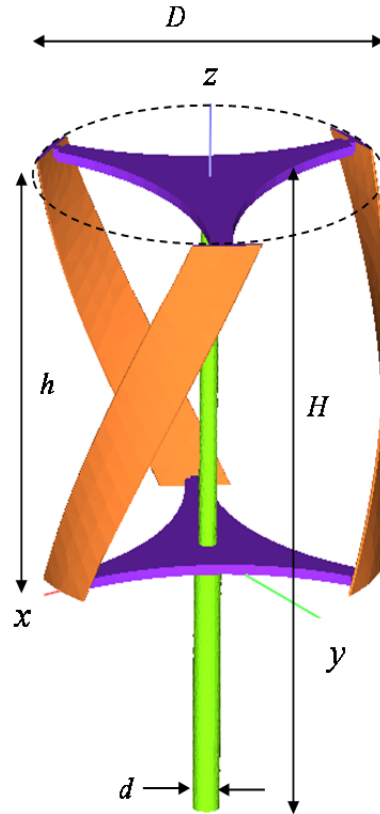
Figure 30. A vertical axis helical model and its dimensions are shown. Different colors indicate different materials used in the CAD model for simulation.

Table 6.   The dimensions of the helical wind turbine configuration.

Vertical axis helical wind turbine
Helix diameter, D = 3 m, height, h = 3 m
Tower height, H = 5 m
Tower diameter at base, d = 0.5 m
Blade width, w = 0.614 m

B. SIMULATION RESULTS FOR THE VERTICAL AXIS HELICAL WIND TURBINE RCS

The monostatic RCS patterns for the helical wind turbine design are shown in Figure 31. All surfaces were set to PEC. The azimuth angle ϕ changes from $0°$ to $360°$, and the elevation angle is set at $\theta = 90°$. The four frequencies selected are representative of wireless, cellular, and radar bands: 400 MHz, 900 MHz, 2400 MHz and 5 GHz. Edge diffraction was not considered in calculating the RCS. The number of rays per wavelength was set to ten. The maximum number of ray bounces was set to five. The incident wave was set to linear polarization.

At the two high frequencies, the rapid oscillations in RCS are due to Bragg scattering from the blades. In general, as the frequency is increased, the phase differences change more rapidly because the distances are longer in terms of wavelength, and the RCS changes faster with angle. The fiberglass monostatic RCS patterns for the helical design wind turbine are shown in Figure 32. The blade surfaces were set to fiberglass. The nacelle and tower surfaces were set to PEC. Compared to Figure 31, the fiberglass blades case has a slightly lower RCS. At higher frequencies, the rapid fluctuations in RCS are due to Bragg scattering from the blades; although, it is not as strong as it is for PEC blades.

Bistatic patterns for the vertical axis helical wind turbine with all metal surfaces, front incident $(\phi_i = 0°)$ and side incident $(\phi_i = 90°)$ waves are shown in Figures 33 and 34, respectively. The forward scattered peaks occur at $\phi = \phi_i + 180°$ in the bistatic patterns in Figures 33 and 34 and are evident at all four frequencies. At the lower frequencies, 400 MHz in particular, the sidelobe structure of the tower is visible. The tower diameter is such that it is in the resonance scattering region at 400 MHz [22]. At 5 GHz, the narrow sidelobes are due to Bragg scattering from the blades.
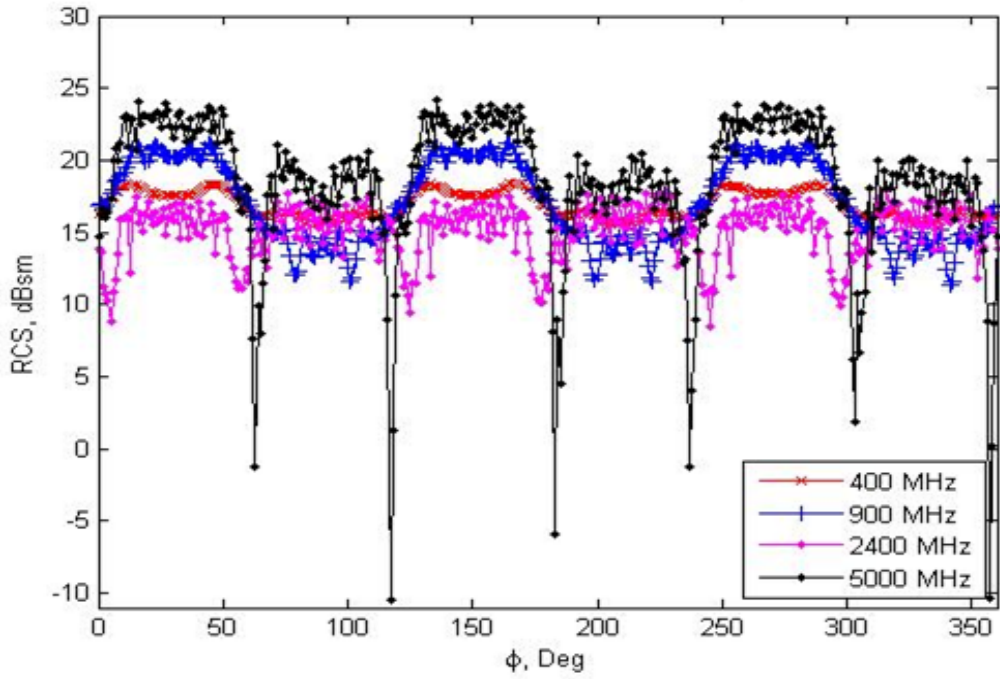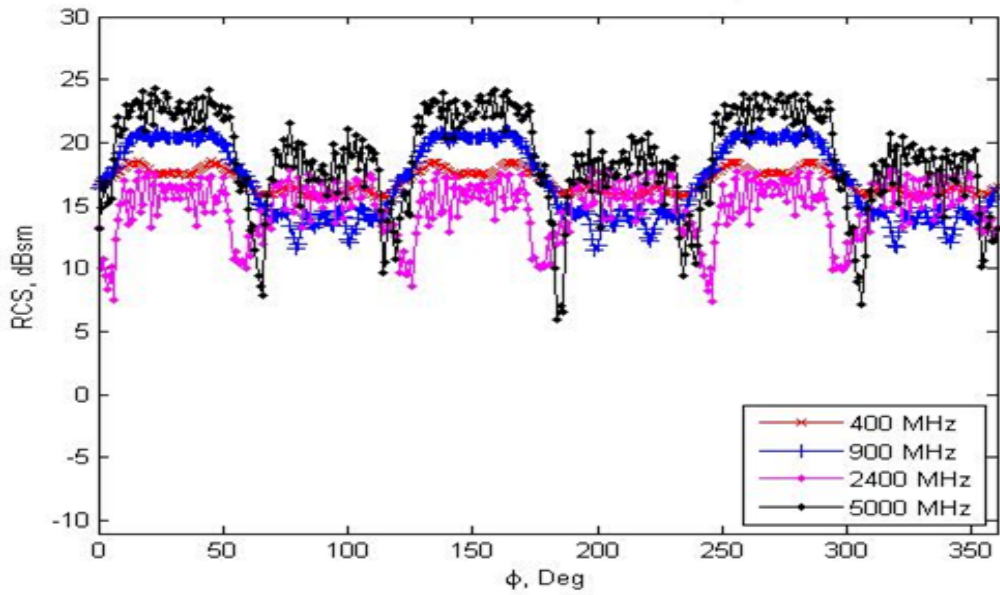
Figure 31. Comparison between four frequencies of monostatic co-polarized RCS of the helical wind turbine with all metal surfaces ($\theta = 90^{\circ}$): (a) $\sigma_{\theta\theta}$, (b) $\sigma_{\phi\phi}$.
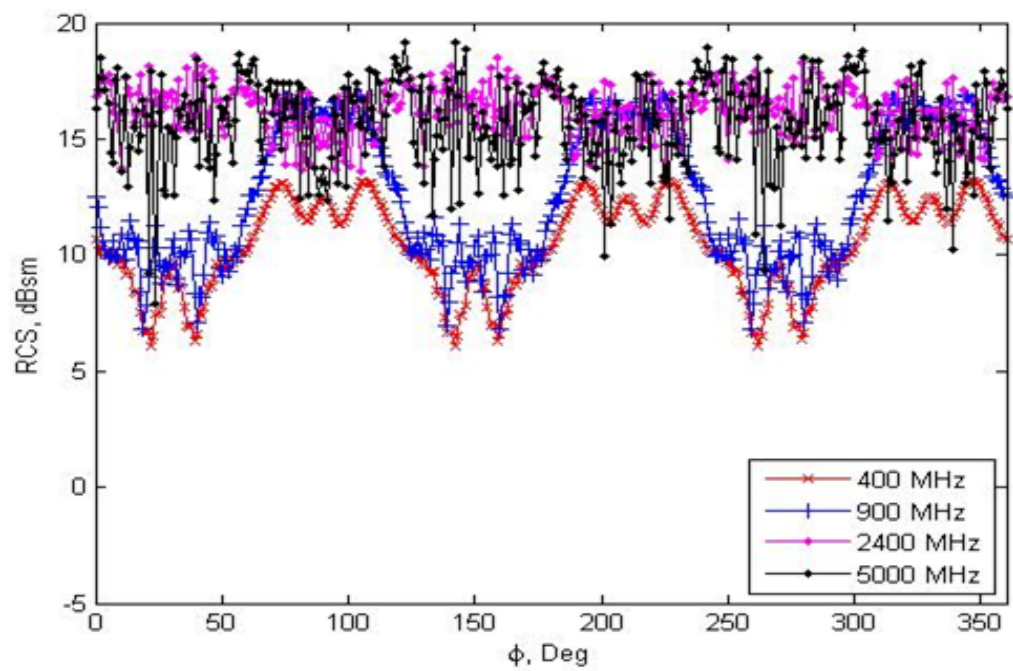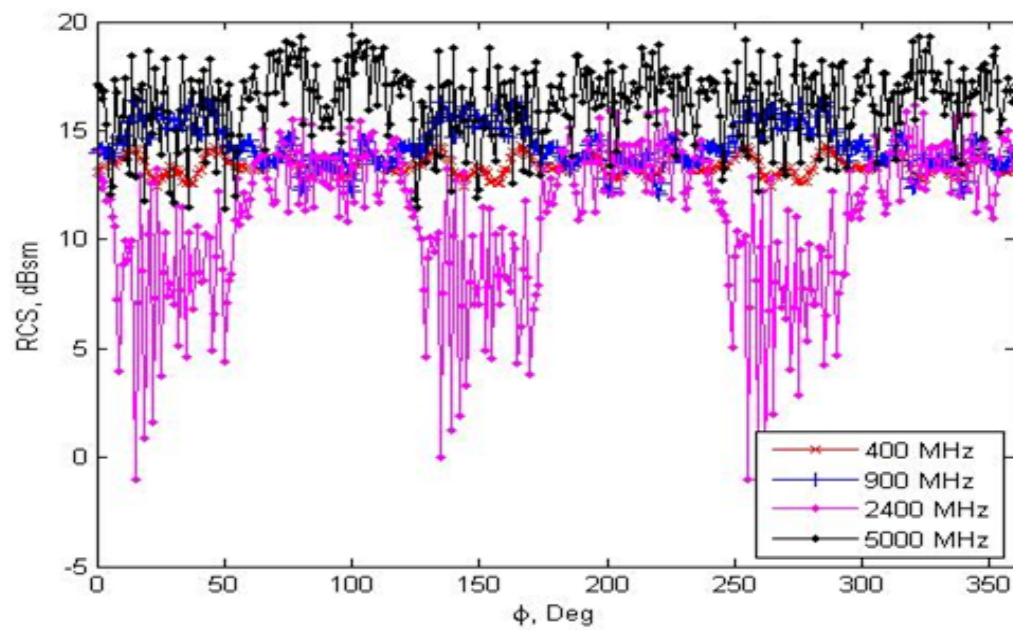
Figure 32. Comparison between four frequencies of monostatic co-polarized RCS of the helical wind turbine with fiberglass blades ($\theta = 90^{\circ}$): (a) $\sigma_{\theta\theta}$, (b) $\sigma_{\phi\phi}$.
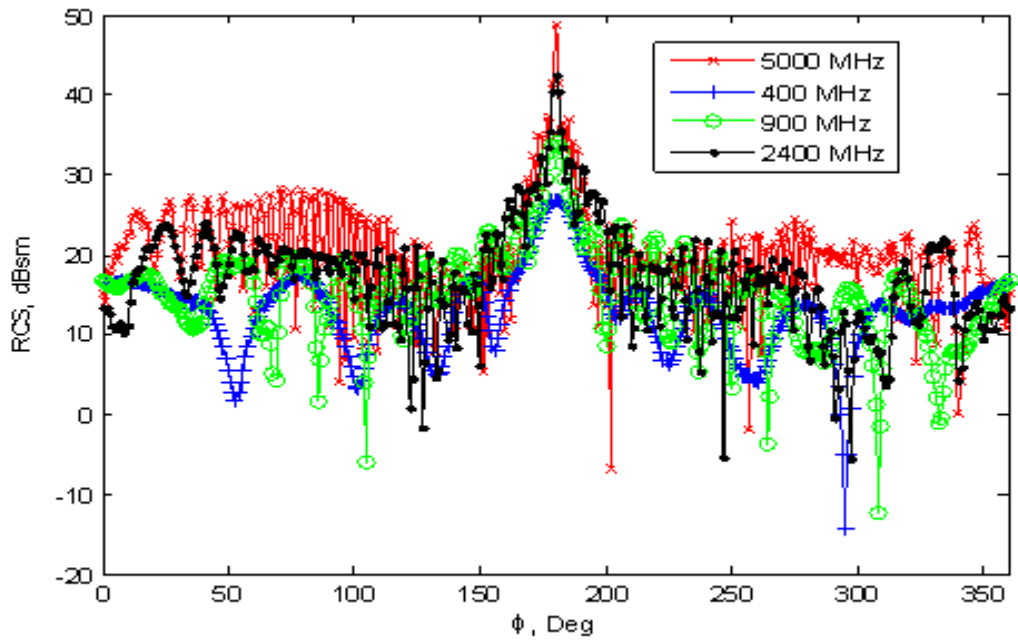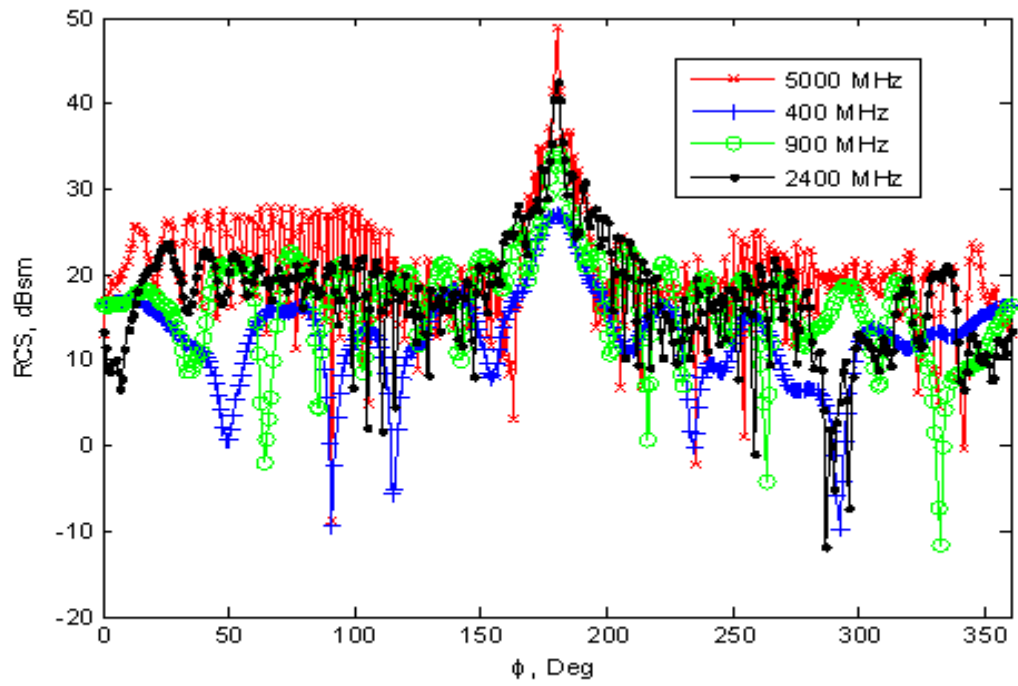
Figure 33. Comparison between four frequencies of bistatic co-polarized RCS of the PEC helical wind turbine, front incidence. ($\theta_i = 90^\circ$, $\phi_i = 0^\circ$, $\theta = 90^\circ$): (a) $\sigma_{\theta\theta}$, (b) $\sigma_{\phi\phi}$.
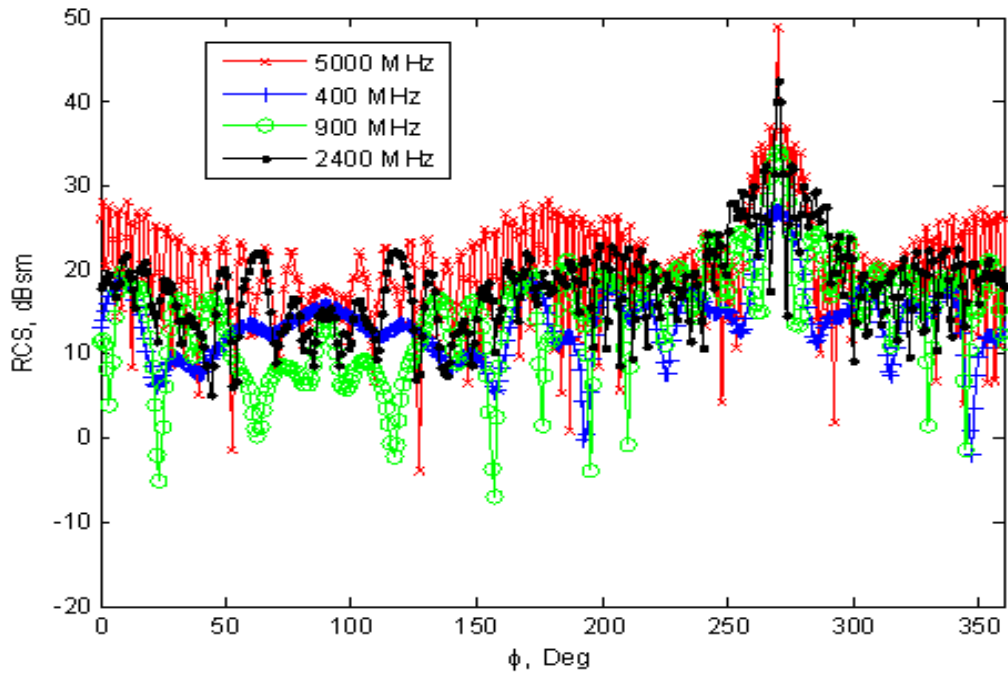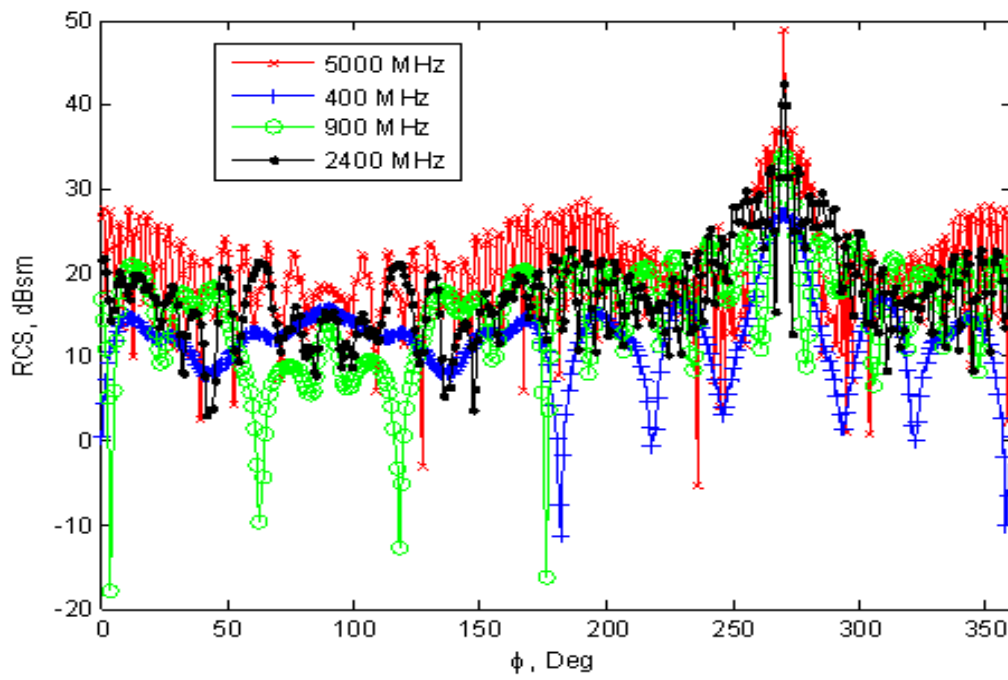
Figure 34. Comparison between four frequencies of bistatic co-polarized RCS of the PEC helical wind turbine, side incidence ($\theta_i = 90°$, $\phi_i = 90°$, $\theta = 90°$): (a) $\sigma_{\theta\theta}$, (b) $\sigma_{\phi\phi}$.

51

In summary, the monostatic and bistatic RCS results of the vertical axis helical wind turbines were presented in this chapter. There are no significant differences in RCS between the PEC and non-PEC cases for the monostatic and bistatic scenarios. At higher frequencies, the rapid fluctuations in RCS are due to Bragg scattering from the blades, which is strongest for PEC blades. In the next chapter, the effect of mesh size and discretization in the CAD model on the convergence of the RCS is analyzed.

VI. COMPUTATIONAL ISSUES

In this chapter, the effects of mesh size and discretization in the CAD model are presented. This is called facetization error. Comparisons between three mesh types (coarse triangular, fine triangular and quadrilateral triangular) are discussed. Monostatic and bistatic RCS results for a horizontal axis wind turbine from four frequencies (400 MHz, 2400 MHz, 2.4 GHz and 5 GHz) with different mesh types are presented to observe the effects of facetization error.

To calculate RCS, the CAD model needs to be meshed into facets. To mesh an isolated large flat rectangular surface CAD model, the software can use a few large triangles to represent this surface accurately. However, if a large surface is part of a complex target with other scattering elements, then the larger surface needs to be segmented into smaller surfaces by the ray tracing algorithm so that blockage and multiple reflections can be accurately determined. In general, the smaller the facets used in the CAD model, the more accurate is the result that the model can generate but the run time increases. In the case of a flat surface, there is a relationship between segmentation and mesh element size. If a large plate is meshed with small triangles, then less segmentation is required by the ray tracer.

An example of how the number of segments used in the CAD model affects the RCS is shown in Figure 35. With adequate segmentation, the perturbation of RCS is relatively small. Only cross-polarized RCS components are likely to be an issue in this case. For curved surfaces, the mesh size must have small triangle edges so that a "tight" fitting mesh can be generated. Even so, when a curved surface is approximated by a triangular mesh, facet noise (facetization error) will occur [40]. In a general sense, facet noise can be categorized as a quantization error that arises from representing the smooth continuous surface with discrete facets.
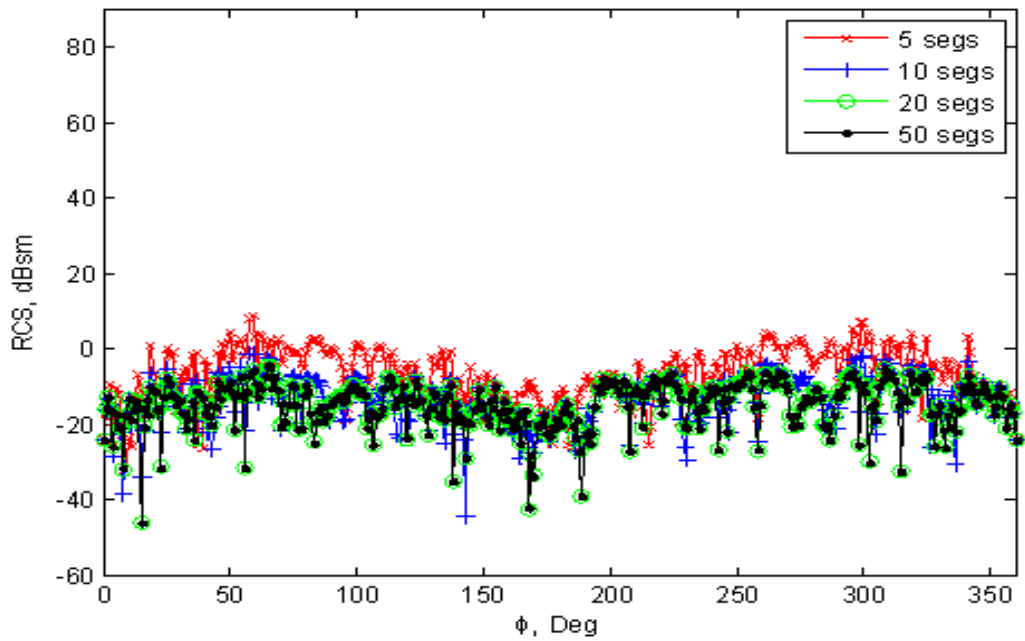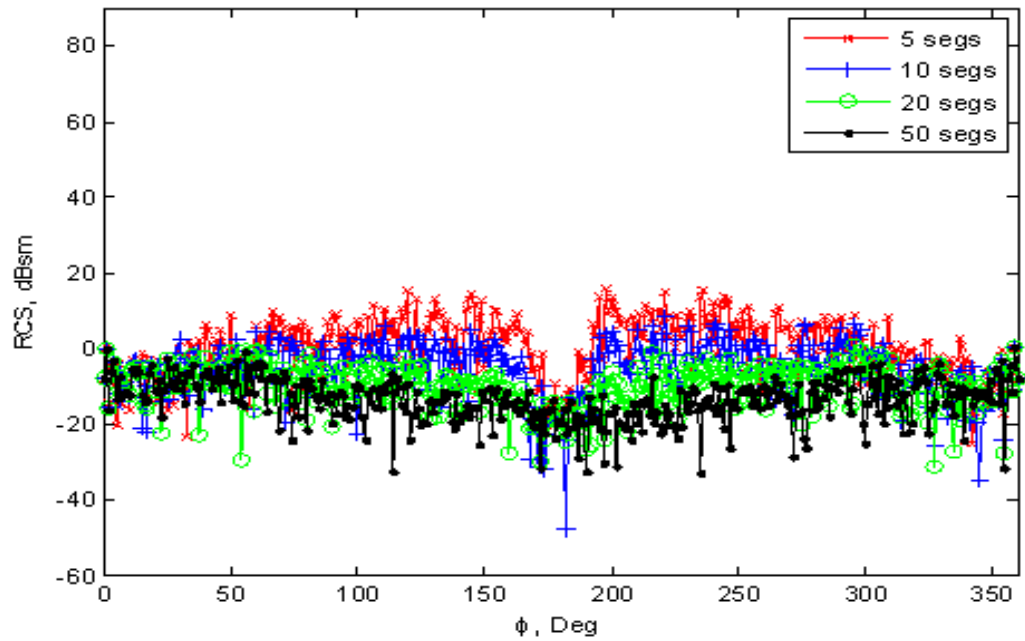
Figure 35. An example of how the segmentation can seriously vary the bistatic azimuth cross-polarized RCS. The data is taken from the PEC horizontal axis wind turbine for incidence from the front ($\theta_i = 90^\circ$, $\phi_i = 0^\circ$, $\theta = 90^\circ$): (a) $\sigma_{\theta\phi}$, (b) $\sigma_{\phi\theta}$.

To observe the effects of facetization error, the monostatic RCS of the PEC tower is calculated at frequency of 900 MHz and shown in Figure 36. Ideally, the monostatic RCS should be constant with angle because the cylindrical shape of the tower has symmetry with the angle ϕ. Notice in Figure 36 that the RCS for the coarse mesh has a 20 dB variation and would generally be considered unacceptable. However, from Figure 18, in the forward scattered direction, the peak RCS level of the bistatic RCS at this frequency is about 70 dB, so this level of facet noise may be acceptable. The RCS for the fine mesh has only a 2 dB variation. As illustrated in Figure 36, the quadrilateral/triangular mesh has the same accuracy as the fine triangular mesh using only 3.7% of the fine mesh's number of facets (4608 facets versus 125240 facets). The reduction yields a significant computational savings when calculating the RCS for the entire wind turbine. The bistatic patterns of the horizontal axis wind turbine for the three meshes at a frequency of 900 MHz are shown in Figure 37. It is evident that the cross-polarized components are more sensitive to facet noise because of the lower values of RCS.
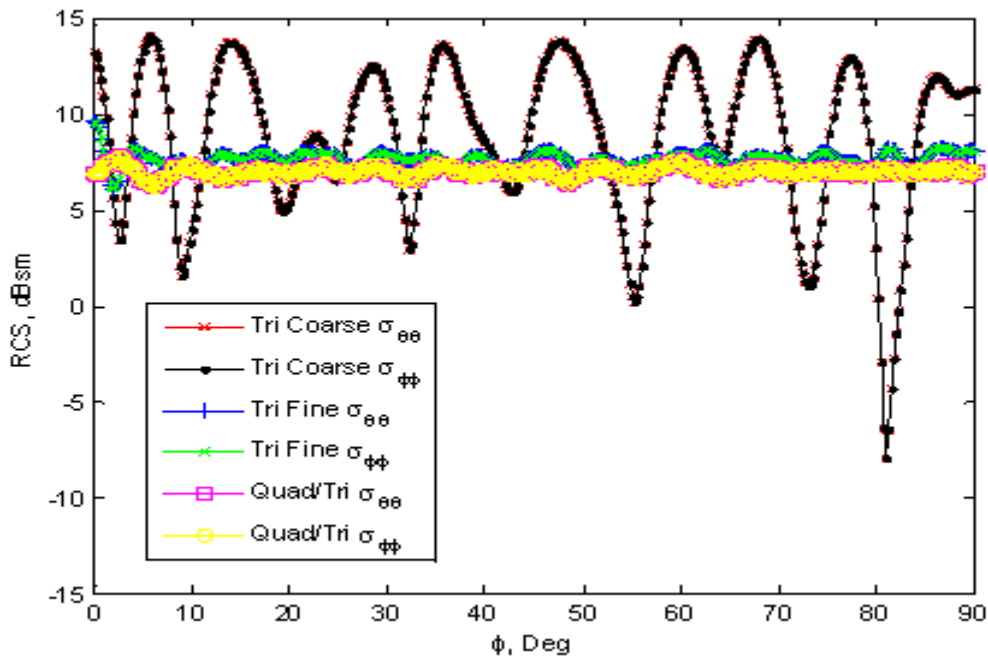
Figure 36. Comparison between the three meshes of azimuth co-polarized monostatic RCS ($f = 0.9$ GHz, $\theta = 90°$) of the PEC tower: coarse triangular (19994 facets), fine triangular (125240 facets) and quadrilateral triangular (4608 facets).
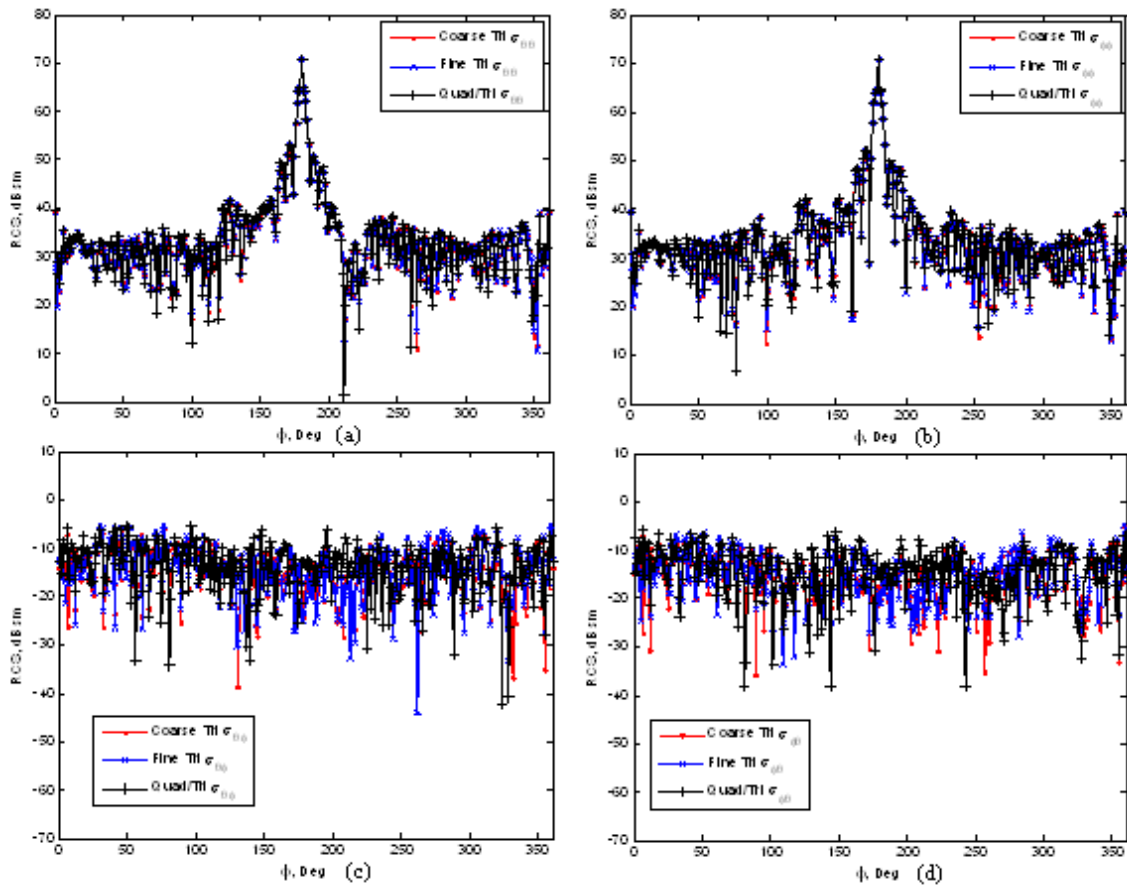
Figure 37. Comparison between four components of bistatic RCS for the three meshes at 900 MHz, all PEC, and front incidence. The cross-polarized components are more sensitive to facet noise because of the lower values of RCS: (a) $\sigma_{\theta\theta}$, (b) $\sigma_{\phi\phi}$, (c) $\sigma_{\theta\phi}$, (d) $\sigma_{\phi\theta}$.

In summary, the effect of mesh segmentation on the convergence of the RCS was discussed. The quadrilateral/triangular mesh is more efficient than the fine triangular mesh and uses only 3.7% of the fine mesh's number of facets. The cross-polarized components are more sensitive to facet noise because of the lower values of RCS. In the next chapter, the focus is on various methods of mitigating wind turbine clutter and approaches to reduce wind turbine RCS.

VII. METHODS OF MITIGATING WIND TURBINE CLUTTER AND REDUCING ITS RCS

In this chapter, several methods of mitigating wind turbine clutter are presented. Various scattering sources and mechanisms from wind turbines are discussed. Several approaches to reduce and control RCS are presented.

A. CLUTTER

Clutter is defined as unwanted signal that originates in the scattering environment and can interfere or mask the desired signal. In the wind turbine case, the SCR is used as the basis for performance evaluation.

One way to mitigate wind turbine clutter is to reduce the wind turbine RCS so that it causes less interference and the SCR is increased. Increasing transmitter power does not help because the clutter return power also increases along with the target power.

In order to increase the SCR, aside from reducing the wind turbine RCS, the sidelobe levels of both the transmitting and receiving antennas should be as low as possible so the gain is lower in the direction of the wind turbine. Also, it helps to operate in an observation direction where the wind turbine RCS is low.

In the case of radar, it is best to operate in a condition where the target range is short and away from the wind farms. This means wind farms are not in the LOS of the radar as depicted in Figure 38. This can prevent scattering interference from the wind farms.

Figure 38. This illustration shows the use of terrain masking as one way to mitigate the impact of wind turbines near a radar site.

In hilly terrain one could use terrain masking by placing wind turbines on the far side of the hill below the peak (non-LOS, Figure 38). However, these areas are generally sheltered from the wind. If wind turbines are in the radar LOS, then fewer, taller wind turbines over a small area may be preferable over many shorter wind turbines in a large area. Another way to mitigate the effect of wind turbines near a radar site is to change the radar pulse repetition frequency to minimize radar signal returns from wind turbines [41]. Also, because wind turbines are generally not efficient at low wind speeds, turning off wind turbines in low wind speeds can also help to minimize wind turbine clutter [41].

In the case of terminal Doppler weather radar (TDWR), as discussed in Chapter IV, Section C, the TDWR sees the Doppler shift returns of the rotating wind turbine blades as targets having reflectivity and motion and, therefore, might process these returns as weather. It is possible to develop a new advanced signal processing technique [42–44] to separate and filter out the wind turbine clutter from the weather signal in the range-Doppler domain. This technique exploits the different spatial and spectral characteristics of wind turbine clutter. Another way to reduce wind turbine clutter is to use adaptive clutter filters in the radar [42–44]. These filter techniques are used combinations with image processing techniques and advanced signal processing techniques to remove or reduce wind turbine clutter. These techniques are complex and can be difficult to implement.

Changing the radar scan strategy so that the radar beam passes over areas with wind turbines will limit the amount of main beam clutter received but will reduce the effective coverage of the radar.

Finally, another way to reduce wind turbine clutter is to reduce RCS of the wind turbine blades by using radar absorbing materials to minimize scattering. This technique is discussed in detail in the next section.

B.   RCS REDUCTION AND CONTROL

To determine how to reduce and control the RCS of a complex object, it is often necessary to examine the bistatic RCS pattern peaks to identify specific scattering mechanisms associated with scattering sources on the target. The electrically large

surfaces of the wind turbine tower and blade are the scattering sources that generate fluctuations in the RCS pattern. Reflections, multipath, diffraction from edges of the blade, surface waves (traveling waves, creeping waves, leaky waves), and Bragg scattering from periodic arrays of scattering elements are examples of scattering mechanisms that can occur in the wind farms scenario. RCS reduction and control techniques are dependent on the scattering sources and mechanisms. For both the monostatic and bistatic cases, the SCR can be increased by reducing the wind turbine RCS as given in (5) and (9). There are three approaches to reducing RCS: shaping, application of radar absorbing materials, and cancellation techniques [21], [22].

Shaping involves the tilting and contouring of surfaces to direct scattered energy away from the interference region; however, reducing RCS at one angle and frequency can lead to larger RCS at other angles and frequencies. Generally, for this approach to be effective, the designer must keep the platform surface flat and smooth so the specular scatterers are confined to a narrow angular region. Shaping applied to the tower and nacelle could be somewhat effective but would have to be done with knowledge of the transmitter and receiver directions. Although it could reduce the RCS in some desired monostatic or bistatic directions, it would likely increase it in others. Shaping of wind turbine structures to reduce RCS has been investigated in [20].

Cancellation techniques include two methods: passive and active cancellation. Passive cancellation is the addition of a secondary scatterer to cancel the reflected field from the wind turbine to induce destructive interference and requires phase coherence between the primary (wind turbine) and secondary scattering components. This is very difficult to achieve, especially at the higher frequencies, and is only effective at limited frequencies and angles. Furthermore, the secondary scatterer has to be very large in order to cancel the large wind turbine RCS. Active cancellation involves methods of regenerating a signal that is 180° out of phase from the wind turbine RCS return so that the total scattered field is zero. This is also very difficult to achieve, especially at high frequencies, because of complex RF circuitry required and processing speed. Both passive and active cancellation methods are limited to narrow bands and spatial regions.

The most compelling and promising approach is the application of radar absorbing material. The material would have to be lightweight, thin, durable, inexpensive, and provide sufficient RCS reduction to make it economically viable. Most commercial RAM materials give a specular RCS reduction in the range of 15 to 20 dB [45] but varies widely with frequency and angle-of-incidence.

A RAM coating can be applied to the surface of the wind turbine. RCS reduction is accomplished by reducing reflections and scattering from the tower and nacelle. One mechanism is by way of absorption, which refers to the transfer of energy from the wave to the material it passes through. The second way is by cancellation of multiple reflections, or destructive interference, where the coating properties are selected so that reflections from the front and back faces of a layer cancel. However, this may add weight to the platform and can affect the aerodynamic performance if applied to the blades. In most situations the aerodynamic degradation and cost would not justify the use of RAM because of the relatively small reduction in RCS that it would provide, but in the case where the radar and communication systems operate near the wind farms, it makes sense to use RAM coating in the wind turbine tower, nacelle, and blades to reduce its RCS.

In summary, several methods of mitigating wind turbine clutter were presented. Mainly, it is advantageous to operate the antenna system in a direction where the wind turbine RCS is low. However, the orientation of wind turbines largely dictated by geographic features and weather phenomena, thereby making this in most cases impractical. In the case of radar, if possible, operate in a condition where the target range is short and in a direction away from the wind turbine. RCS reduction and control techniques are dependent on the scattering sources and mechanisms, but in the case where the radar and communication systems operate near the wind farms, it makes sense to use RAM coating in the wind turbine tower, nacelle, and blades to reduce its RCS. However, this may add weight to the platform and can affect the aerodynamic performance and stability if applied to the blades. The summary, conclusions and recommendations for further research are presented in the next chapter.

VIII. SUMMARY, CONLUSIONS AND RECOMMENDATIONS

A.   SUMMARY AND CONCLUSIONS

The focus of this thesis was to study the scattering behavior and clutter characteristics of two wind turbine configurations: a horizontal axis, three-blade design and a vertical axis helical design. The basic range equations for predicting the scattered power from a wind turbine were covered in Chapter II. In both the monostatic and bistatic cases, we found that SCR can be increased by reducing the wind turbine RCS or operating in a direction where the RCS is low, reducing the antenna sidelobe levels so that the gain is lower in the direction of the wind turbine or, in the case of radar, operating in a condition where the target range is short and in a direction away from the wind farms.

In Chapters III and IV, the approximate high frequency computational methods of SBR and physical optics were used to predict the RCS. The SBR method uses a ray-tracing technique to trace a bundle of incident rays that shoots and bounces throughout the CAD model to find reflection points, diffraction points and shadows. This has the advantage of not requiring the solution of a large number of simultaneous equations. The computational convergence issues related to surface meshing, number of bounces and segmentation of the edges were discussed. The quadrilateral/triangular mesh on the tower provides the same accuracy as a fine triangular mesh with only 3.7% of the fine triangular mesh's number of facets. This reduction yields a significant computational time savings when calculating the RCS for the entire wind turbine.

The behavior of the RCS is a complex function of incident angle, carrier frequency and rotor position. For both wind turbine configurations, simulations showed the following results:

- For bistatic RCS, most forward scattering comes from the tower, and the back scattering comes from the side of the nacelle
- The bistatic forward scatter lobe increases with frequency and is orders of magnitude larger than the backscatter

- Bragg scattering was identified, which originates from a vertical blade and tower

- The sidelobe structure of the tower is visible at the frequency of 400 MHz

- The reduction in RCS by using non-conducting blade materials (fiber glass) is not significant

- A Doppler shift is present when the blade tips move towards or away from the radar location. This Doppler shift can interfere with the receiver processing.

Finally, in Chapter VI, RCS reduction and control for wind turbines by the application of RAM was discussed. In most situations the aerodynamic degradation and cost would not justify the use of RAM given the relatively small reduction in RCS that it would provide. An exception might be when wind farms operate in the vicinity and LOS of radar systems, in which case shaping and RAM can be used effectively.

B.   RECOMMENDATIONS

Further research efforts can be explored to study the scattering behaviors and clutter characteristics of the interactions between large numbers of wind turbines in wind farms. Software algorithms and analytical approaches are needed to model and simulate key interactions that occur when several wind turbines are located near each other as in the case of a large wind farm scenario. Also, nearby buildings and terrain elements could be included in this analysis to further understanding of the effects of the wind turbines on radar performance.

In addition, although there was no significant reduction in RCS using the non-conducting blade materials, the proper selection of the blade material thickness may have some significant RCS reductions. However, changes in the blade shapes have a significant effect on the efficiency of the wind turbine. Further study and simulations on wind turbine RCS with different blade thickness would have to consider aerodynamic efficiency.

LIST OF REFERENCES

[1]   Vesta 1.8 MW wind turbine technical specifications [online]. Available: http://www.vestas.com/Files/Filer/EN/Brochures/V80_18_U.S..pdf, [Accessed January 21, 2013].

[2]   GE Energy 1.5 MW wind turbine technical specifications [online]. Available: http://www.renewableenergysd.com/wp-content/uploads/2011/07/GE-Energy-1.5MW-Wind-Turbine.pdf, [Accessed February 14, 2013].

[3]   http://soaringwindenergy.com/pdfs/BHD%20Brochure.pdf, [Accessed February 14, 2013].

[4]   http://www.quietrevolution.com/qr5/gallery.htm, [Accessed January 21, 2013].

[5]   http://quietrevolution.com/qr5/qr5-turbine.htm, [Accessed February 14, 2013].

[6]   http://www.helixwind.com/en/d361.php#D361specs, [Accessed February 14, 2013].

[7]   http://www.indiamart.com/windivahybrid/vertical-axis-wind-turbines.html, [Accessed February 14, 2013].

[8]   M. Ragheb, *Radar Signatures of Wind Turbine*, ebook, January 18, 2009.

[9]   Michael Brenner, et al., "Wind Farms and Radar," MITRE Corporation, January 2008.

[10]   Office of the Director of Defense Research and Engineering, "The effect of windmill farms on military readiness," Report to the Congressional Defense Committees, U.S. Department of Defense, 2006.

[11]   J. J. Lemmon, et al., "Assessment of the effects of wind turbines on air traffic control radars," U.S. Department of Commerce, July 2008.

[12]   L. Rashid and A. Brown, "RCS and radar propagation near offshore wind farms," *IEEE Antennas and Propagation Society International Symposium*, pp. 4605–4608, June 2007.

[13]   D. Sozen and M. Kartal, "Scatter and Doppler effect of wind power plants to land radars," *14th International Conference on Modeling and Simulation*, *IEEE* Computer Society, pp. 453–458, 2012.

[14] C. Lute and W. Wieserman, "ASR-11 radar performance assessment over a wind turbine farm," *IEEE Radar Conference*, pp. 226–230, 2011.

[15] B. Kent, K. Hill, A. Buterbaugh, G. Zellinski, R. Hawley, L. Cravens, T. Van, C. Vogel, and T. Coveyou, "Dynamic Radar Cross Section and Radar Doppler Measurements of Commercial General Electric Windmill Power Turbines, Part 1: Predicted and Measured Radar Signatures," *IEEE Antennas and Prop. Magazine*, vol. 50, no. 2, pp. 211–219, April 2008.

[16] F. Kong, Y. Zhang, R. Palmer, and Y. Bai, "Wind turbine radar signature characterization by laboratory measurements," *IEEE Radar Conference,* pp. 162–166, 2011.

[17] E. Van Lil, J. De Blesser, and A. Van de Capelle, "Computations on the effects of wind turbines in the close near field of RF installations*," Proc. of the 5th European Conference on Antennas and Propagation* (EUCAP), pp. 1362–1366, April 2011.

[18] Angulo, et al., "Experimental results on wind turbines impact to terrestrial DTV reception in the UHF band," *59th Annual IEEE Broadcast Symposium*, Alexandria, VA, 14–16 October 2009.

[19] L. Rashid and A. Brown, "Radar cross section analysis of wind turbine blades with radar absorbing material," *Proc. of the 8th European Radar Conference*, pp. 97–100, 12–14 October 2011.

[20] J. Pinto, J. Matthews, and G. C. Sarno, "Stealth technology for wind turbines," *IET Radar Sonar Navigation*, vol. 4, no. 1, pp. 126–133, 2000.

[21] E. Knott, J. Shaffer, and M. Tuley, *Radar Cross Section*, 2nd ed. London: Artech House, 1993.

[22] D. Jenn, *Radar and Laser Cross Section*, 2nd ed., Reston, VA: AIAA Education Series, 2005.

[23] M. I. Skolnik, *Introduction to Radar Systems*, 3rd ed. New York: McGraw-Hill, December 2002.

[24] D. C. Jenn and C. Ton, "Wind turbine radar cross section," *International Journal of Antennas and Propagation*, vol. 2012, 2012.

[25] W. Stutzman and G. Thiele, *Antenna Theory and Design*, 2nd ed., Wiley, 1998.

[26] N. Willis, *Bistatic Radar*, 2nd ed. London: Artech House, March 2005.

[27] C. Balanis, *Advanced Engineering Electromagnetics*. New York: McGraw Hill, May 1989.

[28] K. Kunz and R. Luebbers, *The Finite Difference Time Domain Method for Electromagnetics*, Boca Raton, FL: CRC Press, 1993.

[29] J. Volakis, A. Chatterjee, and L. Kempel, *Finite Elements Method for Electromagnetics*, Hoboken, NJ: Wiley/IEEE Press, 1998.

[30] H. Ling, R. C. Chou, and S. W. Lee, "Shooting and bouncing rays: calculating the RCS of an arbitrarily shaped cavity," *IEEE Trans. on Antennas and Prop.,* vol. AP-37, no. 2, pp. 194–205, February 1989.

[31] ANSYS HFSS web page [online]. Available: http://www.ansys.com/ [Accessed January 4, 2013].

[32] CST MWS web page [online]. Available: http://www.cst.com/Content/Products/MWS/Overview.aspx [Accessed January 5, 2013].

[33] FEKO web page [online]. Available: http://www.feko.info/product-detail/overview-of-feko [Accessed February 18, 2013].

[34] XGTD web page [online]. Available: http://www.remcom.com/xgtd/ [Accessed February. 18, 2013].

[35] Tripoint Industries web page [online]. Available: http://lucernhammer.tripointindustries.com/ [Accessed January 5, 2013].

[36] 3D Content Central, CAD model web page [online]. Available: http://www.3dcontentcentral.com/Search.aspx?arg=wind%20turbine [Accessed January 5, 2013].

[37] U.S. Air Force Research Laboratory Supercomputing Resource Center web page [online]. Available: http://www.afrl.hpc.mil/software/info/acad/#desc [Accessed January 5, 2013].

[38] "Fiberglass compositions and their comparative properties," *Ceramic Industry*, http://www.ceramicindustry.com/ext/resources/CI/Protected/Files/PDF/fiberglass-compositions.pdf [Accessed January 5, 2013].

[39] Brian C. Howard, "Helix collapse fails to crush hope for vertical wind turbines," National Geographic Daily News [online]. Available: http://news.nationalgeographic.com/news/energy/2012/08/120820-helix-wind-collapse/ [Accessed January 5, 2013].

[40]   E. Miller, D. Andersh, and A. Terzuoli, "The effect of target model facetization on RCS predictions," *IEEE Antennas and Propagation Society International Symposium Digest*, pp. 1404–1407, 1993.

[41]   S. Turner, "QinetiQ report on impact of the PdV wind farm on RCS measurements at the Tejon Range," QinetiQ, July 2007.

[42]   S. Bachmann, Y. Al-Rashid, B. Isom, and R. Palmer, "Radar and wind farms: mitigating negative effects through signal processing," *The Sixth European Conference on Radar in Meteorology and Hydrology*, ERAD, Sibiu, Romania, pp. 81–86, 2010.

[43]   B. Gallardo, F. Pérez, and F. Aguado, "Characterization approach of wind turbine clutter in the Spanish weather radar network," *The Fifth European Conference on Radar in Meteorology and Hydrology*, ERAD, Helsinki, Finland, 2008.

[44]   F. Nai, R. Palmer, and S. Torres, "Wind turbine clutter mitigation using range-Doppler domain signal processing method," *27th Conference on Interactive Information and Processing Systems*, American Meteorological Society, Seattle, WA, 2011.

[45]   Emerson and Cuming web page [online]. Available: http://www.eccosorb.com/products-eccosorb-fgm.htm [Accessed January 8, 2013].

INITIAL DISTRIBUTION LIST

1.   Defense Technical Information Center
        Ft. Belvoir, Virginia

2.   Dudley Knox Library
        Naval Postgraduate School
        Monterey, California